ISTANBUL TECHNICAL UNIVERSITY ★ GRADUATE SCHOOL OF SCIENCE ENGINEERING AND TECHNOLOGY

EFFECT OF CHAMFERED NOZZLE GEOMETRY ON IMPINGING JET FLOW

M.Sc. THESIS

Araz JABBARLI

Department of Aeronautics and Astronautics Engineering

Aeronautics and Astronautics Engineering Program

SEPTEMBER 2018

ISTANBUL TECHNICAL UNIVERSITY ★ GRADUATE SCHOOL OF SCIENCE ENGINEERING AND TECHNOLOGY

EFFECT OF CHAMFERED NOZZLE GEOMETRY ON IMPINGING JET FLOW

M.Sc. THESIS

Araz JABBARLI
511151165

Department of Aeronautics and Astronautics Engineering

Aeronautics and Astronautics Engineering Program

Supervisor: Assist. Prof. Dr. Duygu ERDEM

SEPTEMBER 2018

ISTANBUL TEKNİK ÜNİVERSİTESİ ★ FEN BİLİMLERİ ENSTİTÜSÜ

DARALAN LÜLE GEOMETRİSİNDE PAH KIRMANIN ÇARPAN JET AKIM YAPISINA OLAN ETKİSİ

YÜKSEK LİSANS TEZİ

Araz JABBARLI
511151165

Uçak ve Uzay Mühendisliği Anabilim Dalı

Uçak ve Uzay Mühendisliği Programı

Tez Danışmanı: Dr. Öğr. Üyesi Duygu Erdem

EYLÜL 2018

Araz JABBARLI, a M.Sc. student of İTU Graduate School of Science Engineering and Technology student ID 511151165, successfully defended the thesis/dissertation entitled "EFFECT OF CHAMFERED NOZZLE GEOMETRY ON IMPINGING JET FLOW", which he prepared after fulfilling the requirements specified in the associated legislations, before the jury whose signatures are below.

Thesis Advisor :	**Assist. Prof. Dr. Duygu ERDEM** İstanbul Technical University	.....
Jury Members :	**Assist. Prof. Dr. Duygu ERDEM** Istanbul Technical University	.....
	Assist. Prof. Dr. K. Bülent YÜCEİL Istanbul Technical University	.....
	Assist. Prof. Dr. Özgür ERTUNÇ Özyeğin University	.....

Date of Submission : 11 September 2018
Date of Defense : 26 September 2018

To my family and my niece Sara,

FOREWORD

I am greatful for the the guide and help that my advisor Duygu Erdem has provided during my graduate studies. And I mostly owe a great thank to the Reasearch Assistant Yavuzer Karakuş who helped me in every stage of the thesis. Additionally, beyond any doubt, without constant encouragement and support from my familiy and friends, this would not be possible.

September 2018 Araz JABBARLI

TABLE OF CONTENTS

ABBREVIATIONS

RIT	**:** Rotor Inlet Temperature
ISO	**:** International Organization for Standardization
PID	**:** Proportional-Integral-Derivative
NI	**:** National Instruments
CA	**:** Connector Accessory
DAQ	**:** Data Acquisition

SYMBOLS

p/e	**:** pitch to height ratio
H/d_n	**: (or e/d_n)** Nondimensional jet-to-target spacing
U_{max}	**:** Maximum velocity
U	**:** Mean velocity obtained from hot-wire measurments
q_m	**:** Air flow rate
r/d_n	**:** Nondimensional radial distance from center of jet
D	**:** Pipe diameter
d	**:** Jet diameter
d	**:** Orifice diameter
L_1	**:** Distance of the upstream tapping from the upstream face of the orifice plate
L'_2	**:** Distance of the downstream tapping from the downstream face of the orifice plate
ρ	**:** Density
C	**:** Discharge coefficient
ε	**:** Expansion factor
β	**:** Orifice diameter to pipe diameter ratio
Δp	**:** Pressure difference
Re_D	**:** Reynold's number of orificemeter pipe
$L_{h_{turbulent}}$	**:** Entrance length
μ	**:** Dynamic viscosity of air
Ma	**:** Mach number
a	**:** Speed of sound
γ	**:** Specific heat ratio
R	**:** Gas constant for dry air
T	**:** Air temperature
x/d_n	**:** radial distance
y/d_n	**:** axial distance
U^*	**:** Mean velocity obtained from flowrate control
U_c	**:** Centerline velocity

LIST OF TABLES

LIST OF FIGURES

EFFECT OF CHAMFERED NOZZLE GEOMETRY ON IMPINGING JET FLOW

SUMMARY

The widespread usage of impingement cooling makes this technique popular. From simple hand drier to advanced gas turbine, most of the industries use this technique for drying or cooling. Therefore, many studies both experimental and numerical are conducted to study every aspect of this technique. However, for optimum usage of this technique, the affecting parameters should be analyzed and designed accordingly. There are important parameters, which directly influences the heat transfer efficiency of jet impingement. These nozzle parameters are Reynolds number, depending on the flow speed and sizing of the jet nozzle, Mach number, jet-to-target spacing, jet-to-jet spacing and finally jet geometry. So far, variety of geometries have been tried and analyzed to study the flow structures and contribution to the heat transfer. Because, studying the flow structures would bring us at the end to the optimum shape of efficient heat transfer by impinging jet technique.

Through this study another jet geometry, which is the chamfered, was studied. The experimental study was conducted by 0^0, 30^0 and 45^0 chamfered nozzles for two different Reynolds number (9,600 and 19,200) and for three different jet-to-target spacings (H/d_n = 4, 6, 10) to observe the effect of these parameters. To understand the flow field, hot wire anemometer measurements were conducted and backed up with pressure measuerements.

DARALAN LÜLE GEOMETRİSİNDE PAH KIRMANIN ÇARPAN JET AKIM YAPISINA OLAN ETKİSİ

ÖZET

Çarpan jet akışının ünlü ve çok çalışlan teknik olma nedeni çeşitli endüstriel alanlarda kullanılmasıdır. Basit kurutuculardan gelişmiş gaz türbinlerine kadar tüm alanlarda kullanılmaktadır. Bu nedenden dolayı şimdiye kadar hem sayısal hem de deneysel çalışmalarla bu teknik incelenilmiştir. Çarpan jet akışınn yapısının öğrenilmesi, bu tekniği verimli bir şekil uygulamasını da beraberinde getirecektir. Şimdiye kadarki çalışmalarda farklı parametreleri incelenmiştir. Bu parametreler, Reynolds sayısı, Mach sayısı, jet'le hedef arası mesafe ve çoklu jet durumunda jetler arası mesafe'dir. Buna ilave olarak, farklı jet geometrilerini incelenmesi üzerine de çalışmalar yapılmıştır. Bu çalışmada da daralan lüle geometrisinde pah kırmanın akış yapısına oan etkisi incelenmiştir. Üç farklı açı incelenmiştir. Bunlar 0^0, 30^0 ve 45^0'dir. Açı deyişimine ek olarak, tüm deneyler iki farklı Reynolds sayısı (9,600 ve 19,200) ve üç ayrı jet'le hedef arası mesafede (H/d_n = 4, 6, 10) yapılmıştır. Akış yapılarını incelemek adına, sıcak tel analizleri de yapılmış ve basınç dağılımı verileriyle desteklenmiştir.

1. INTRODUCTION

1.1 Jet Impingement Background

Jet impingement is a widespread means of cooling, heating or drying, from simple hand, sheet of papers and textile drying machines (Polat, 1993) to a turbine cooling of gas turbine engines (Han, 2013). Due to the effectiveness of achieving high heat/mass transfer in any surfaces, jet-impinging flow is an attractive technique for many industries. In addition to the high heat/mass transfer, this flow also gives the designer a high degree of control of the surface heat transfer rate and distribution (Angioletti, 2002). Depending on the industrial application, the jets are assigned from the array of jet holes, which impinge on the aimed surface to accomplish considerably enhanced convective heating, cooling, or drying characteristics. This is the direct outcome of the flow characteristics of the jet-impinging flow.

In general, an impinging jet can be divided into three main regions; free jet region, the stagnation region, and the wall jet region. Figure-1.1 presents the structure of an impinging jet.

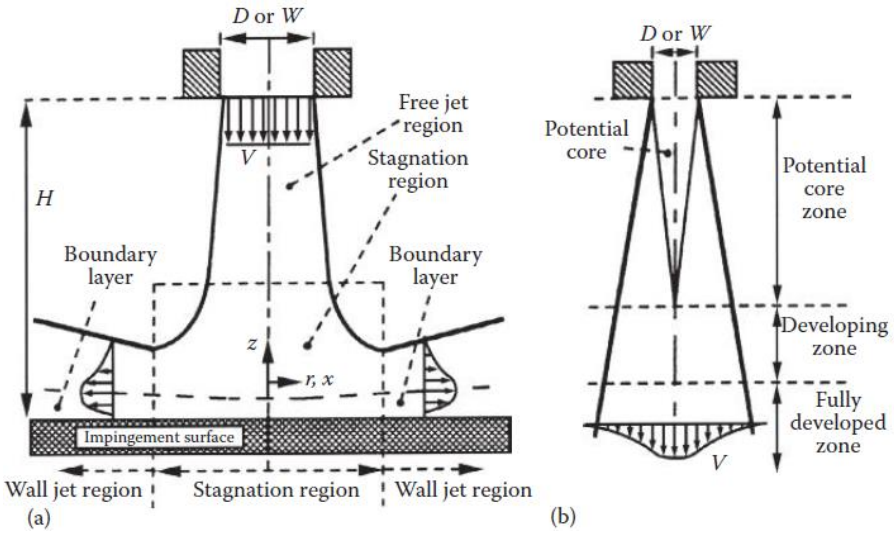

Figure 1.1 Structures of Impinging Jet (Han, Dutta and Ekkad, 2013)

The free jet region is the region right after the gas leaves the jet orifice and starts to mix with surrounding air. This would increase the jet diameter and flow turbulence (Uysal et al., 2014). The flow region within the free jet that is unaffected by the surrounding is called the potential core where the velocity distribution is uniform and equals to the jet exit velocity (Jordan et al., 2012). As the distance between jet orifice and target plate increases, the potential core diminishes. The reduction of the potential core is the direct consequence of the momentum exchange with the relatively stationary ambient air, and the growth of shear layer around jet. Momentum loss to the surrounding air leads to the spreading the bounds of the free jet radially which leads to the shrinkage of the potential core. The contraction in potential core continues until the spacing between jet-to-target is large enough that the potential core fully dissipate (Jordan et al.,2013). Turbulent mixing which is stimulated by shear layer, is also another agent that aids the reduction of the potential core. After dissipation of the potential core, mixing with the stagnant air continue by further reduction in jet velocity relatively far from the exit. Then comes the stagnation region, where the free jet slows down due to the target surface and then it spreads in the radial direction and accelerates outwards from the centre of the jet, parallel to the target surface. This is the region where the heat transfer is maximum at first but decreases as it travels further. As the fluid particles encounter the stationary target surface and due to the rapid acceleration outward, the stationary particles of the surface force the fluid particles to slow down and almost go to zero at the surface. Starting from the zero condition of the velocity in the target surface, the velocity differences of the flow layers, gives rise to a boundary layer which is the another region of an impinging jet, wall jet region. Generation of the wall jet due to the rapid acceleration is displaced by deceleration, which is the direct result of the entrainment with the ambient air.

1.2 Gas Turbine Engine Application

Gas turbine engines are the power generation systems that are mostly used in aircraft as a propulsion system and the land based power generation for generating the large and small-scale power. The simple operational principle of the gas turbine engines can be defined with four words. These are suck, squeeze, burn and blow. The fan or the low-pressure compressor draws a huge volume of air into the engine and accelerates it to the high-pressure compressor where the introduced air is compressed to gain energy.

The massively compressed air passes to the combustion chamber where the compressed air is mixed with the fuel and burned up to 2300^0 C (Han, 2013). Then comes the stage of blow where the hot gases from the combustion chamber goes through a series of stationary turbine vanes and rotating turbine blade to extract energy from high temperature and high-pressure flow. This is the whole process which provide power or propulsion. The general scheme of gas turbine engine is shown in the **Figure-1.2**.

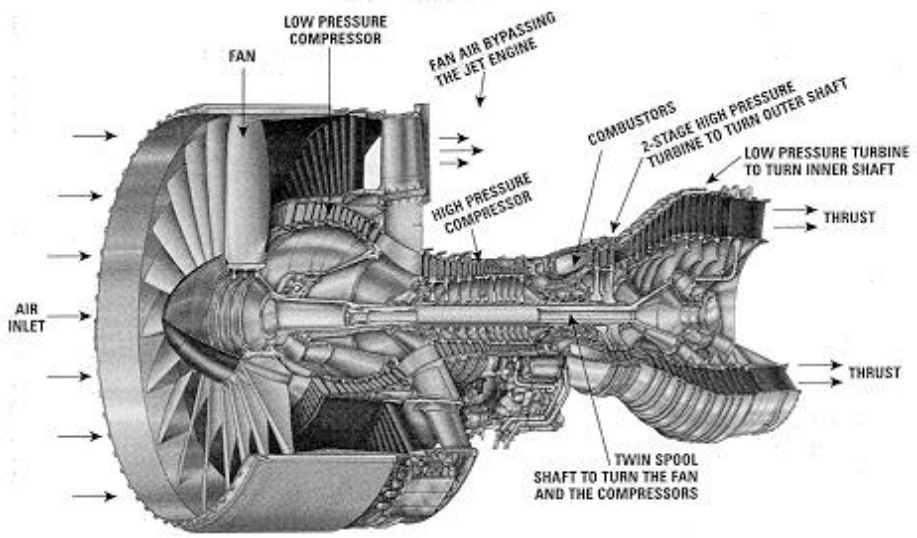

Figure 1.2 Gas Turbine Engine (The Pratt and Whitney 4084 (Drawing Courtesy of Pratt and Whitney))

In order to extract maximum power from the gas turbine, two parameters should be taken into consideration. First is the compression ratio of the compressor stage and the second is turbine rotor inlet temperature (RIT). Therefore, increasing either of them would make the engine to generate more thrust or power. Dependence of turbine inlet temperature with power output can be seen from the **Figure-1.3** that as the RIT increases, the specific core power increases.

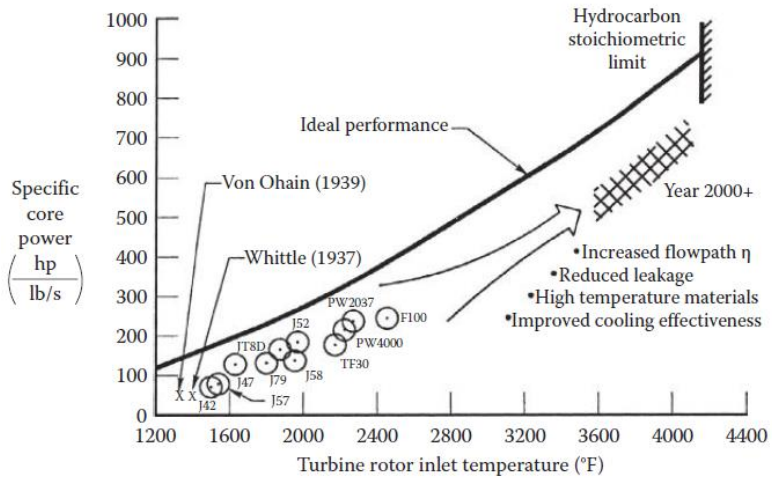

Figure 1.3 The Effect of Rotor Inlet Temperature on Turbine Power Output (Han, Dutta and Ekkad, 2013)

Therefore, a lot of effort was put into increasing the RIT temperature. Today, turbine blades can withstand around 1500^0 C, which is far higher than the melting point of the blade material (SUNDEN and XIE, 2010). This requires the proper cooling system, which would also eliminate the thermal stresses and increase operational life span. The variation of the rotor turbine inlet temperature over the year can be seen in the **Figure-1.4**.

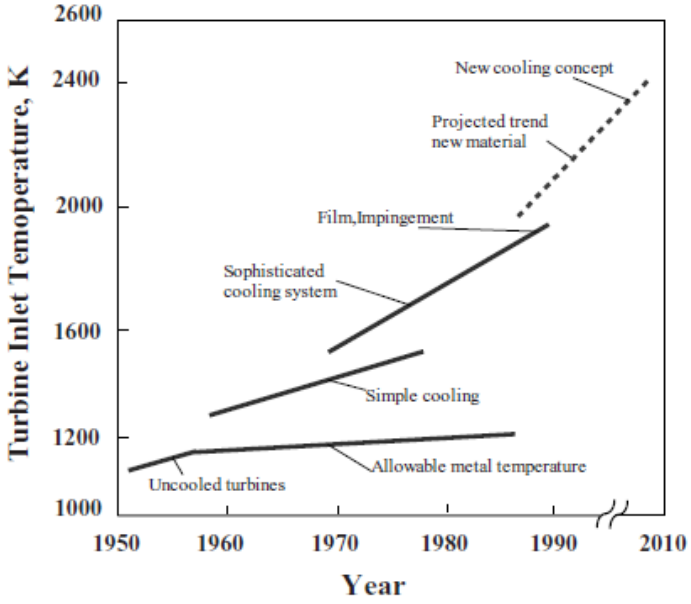

Figure 1.4 Improvement of Turbine Inlet Temperature with Years (SUNDEN and XIE, 2010)

Advanced gas turbine engines are using two techniques to cool the turbine blades, these techniques are film cooling which interprets the external cooling, and internal cooling. For the external or the film cooling, the extracted bleed air from the compressor stage air is injected to the inside of the blade where the air is ejected to the outside surface, which forms a protective layer between the blade surface and hot mainstream. In this technique, the care must be taken to regulate the coolant air to the mainstream, which can significantly drop the temperature of the working fluid; this at the end can lead to the reduction of power output from the turbine. In addition, internal cooling technique can be divided into four, mid-chord rib turbulated cooling, blade tip internal cooling, trailing edge pin fins cooling and leading edge jet impingement cooling. In mid-chord rib turbulated cooling, which is depicted in **Figure – 1.5**, the injected air pass through the channel where the different sizes of the ribs are cast in opposite walls of internal coolant passages to increase the heat transfer. The rib turbulators or another words turbulence promoter causes a flow separation, which increases the flow turbulence and reattach the boundary layer to the surface (Han, 2012). As a result, the mixing is increased due to the rise of turbulence and separated boundary layer, which augments the heat transfer coefficient from the surface to the main flow. The only drawback is the pressure drop in the main flow in the near wall but this penalty is acceptable for blade cooling designs. Most of the time, the nearly square geometry is used for the repeated ribs. The effecting parameters of the rib turbulators are mainly, the coolant channel hydraulic diameter (e/P), a rib spacing-to-height ratio (p/e) and a rib flow-attack-angle.

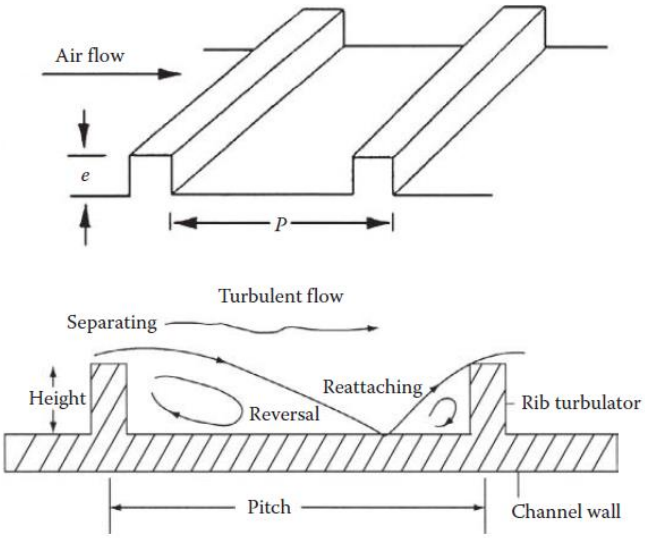

Figure 1.5 Schematics of Rib Turbulators. (Han, Dutta and Ekkad, 2013)

In gas turbine engines, rotating blades have a clearance or the gap between casing or the shroud, which allows the rotation of the blades and allows mechanical and thermal expansion (SUNDEN and XIE, 2010). However, generated pressure difference between pressure side and suction side in the turbine blade causes the hot gas leak through the gap. This leakage causes both reduction in the overall efficiency due to the generated secondary flow, and higher heating at the high-pressure tip corner from mid-chord to trailing edge. To overcome the local heat load in the tip, the extracted air from the compressor stage passing through the internal channel of the blade reaches to the tip-cap of the turbine blade where the flow convectively removes the heat internally and externally. The detailed scheme of the blade tip cooling can be seen in the **Figure-1.6b**.

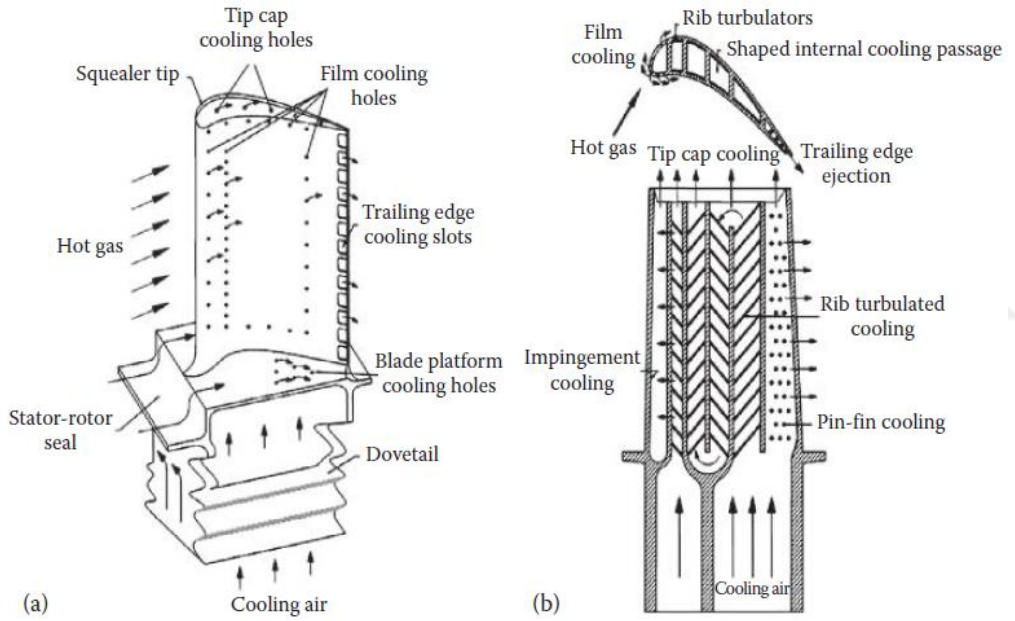

Figure 1.6 Turbine Blade a) External and b) Internal Cooling Schematics (Chyu and Siw, 2013)

Furthermore, as seen from the Figure-3b where one can see that in addition to the mentioned cooling techniques, there is also a trailing-edge pin fins cooling. This cooling technique is similar to the rib turbulated cooling technique but in this one, the common use of geometries are the decrescenting cylinders, which can be seen in **Figure-1.7**. The idea behind the pin fin cooling is that the pins that are casted to the limited area in the trailing edge, enhances the turbulence to increase the heat transfer

from the end-walls and cylinders. Lots of study were done to investigate the effect of the geometry and distribution of pin fins on heat transfer.

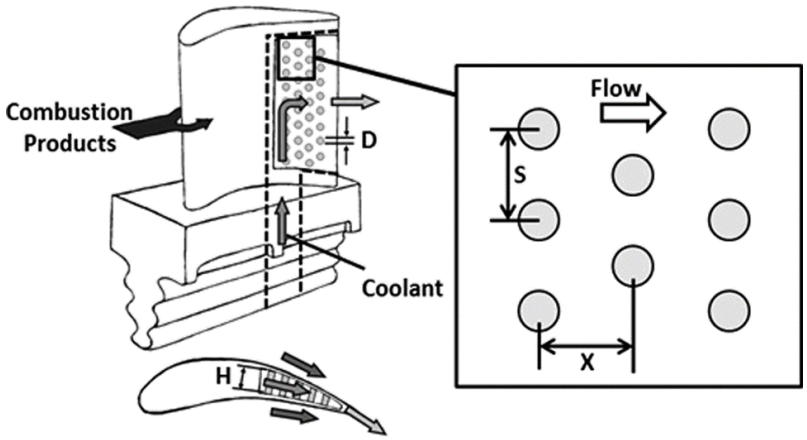

Figure 1.7 Trailing-Edge Pin Fins Cooling Schematic (Ostanek, 2014)

Finally, the last cooling technique is the impingement cooling which is the most aggressive form of cooling. This technique is often used within the leading edge of the turbine blade where the thermal load is highest and therefore this portion of the blade can properly accommodate impingement cooling (Han 2013). The air that is drawn from the compressor stage is directed radially to the plenum where the flow turns axially and blown to the target surface by holes in the inner surface of the turbine, **Figure – 1.8**. In addition to usage of impingement cooling technique in blades, this technique is also widely used in cooling the combustion chamber liners in gas turbine (Bailey, 2002) and in other industries like electrical equipment cooling, paper and textile drying and rocket launcher cooling (Shanley, 2011).

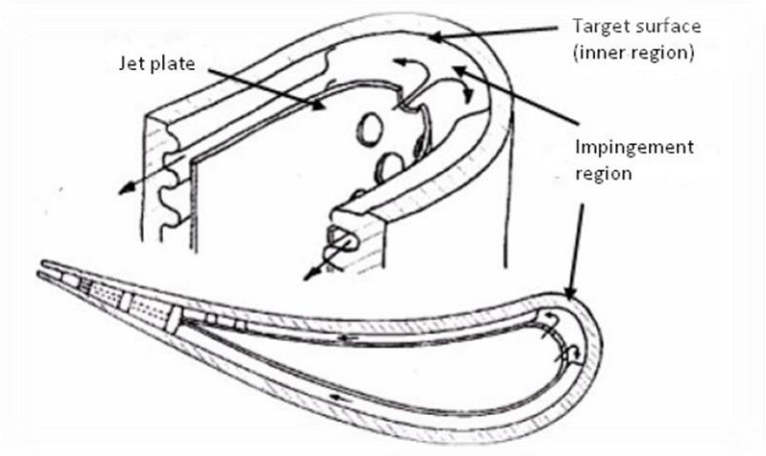

Figure 1.8 Jet Impingement Cooling in Leading Edge of Turbine Blade (Uysal et al., 2014)

Impingement cooling is defined by several parameters that affects the heat transfer in the target surface. These parameters are jet diameter, jet geometry, spacing between jets, spacing between jet and target, channel cross-section and spent-air cross flow. Up to now, lots of single and multi-jets with different geometries were attempted in majority of literature. In addition, little work has done to realize the effect of chamfered jet nozzles on jet flow characteristics. Therefore, the following thesis aims to present the pressure distribution associated with the multi-jet chamfered nozzle geometries. The study has been conducted in the newly designed jet impingement test set-up. Three different chamfer angles were considered; 0^0 which is the traditional circular geometry, 30^0 and 45^0. In addition to the chamfer angles, different Reynolds numbers and jet-to-target spacing were considered. The local measurements of the flow velocity were done by hot-wire anemometer.

1.3 Experimental Set-up

Experimental set-up was constructed with the resources that was provided by the Trisonic Research Laboratory, within the body of Faculty of Aeronautics and Astronautics at Istanbul Technical University. The experimental facility is intended to simulate the simplest condition in an impingement cooling technique similar to those found in modern, actively cooled, turbine airfoils. Test section is comprised of six main parts; compressed air tank, main feeding valve, pressure regulator, ball valve with actuator, orifice meter and pressure chamber. The general scheme of the set-up is shown in the **Figure-1.9** and the constructed set up is shown in the **Figure – 1.10**. Air tank is filled with the external compressor for constant use that can hold maximum 40 bar of compressed air. Main feeding valve allows the airflow to the main pipeline and with the help of pressure regulator; the flow pressure is regulated so that it cannot exceed the certain desired pressure level. The model of the regulator is Accu Aire. Then comes the orifice meter which helps to get pressure difference for controlling the air flow entering to the pressure chamber where the flow is extracted and impinged from the multi in-line jets to the target surface. The old version of the set-up was inherited by the previous thesis work but due to the experimentation differences and raised problems by the old version, the orifice meter, pressure scanner and the

supporting frames were designed and manufactured from the very beginning. Additionally, the proper controlling LabVIEW program was written and implemented which can be found in Control and Data Acquisition (LabVIEW) part of the thesis.

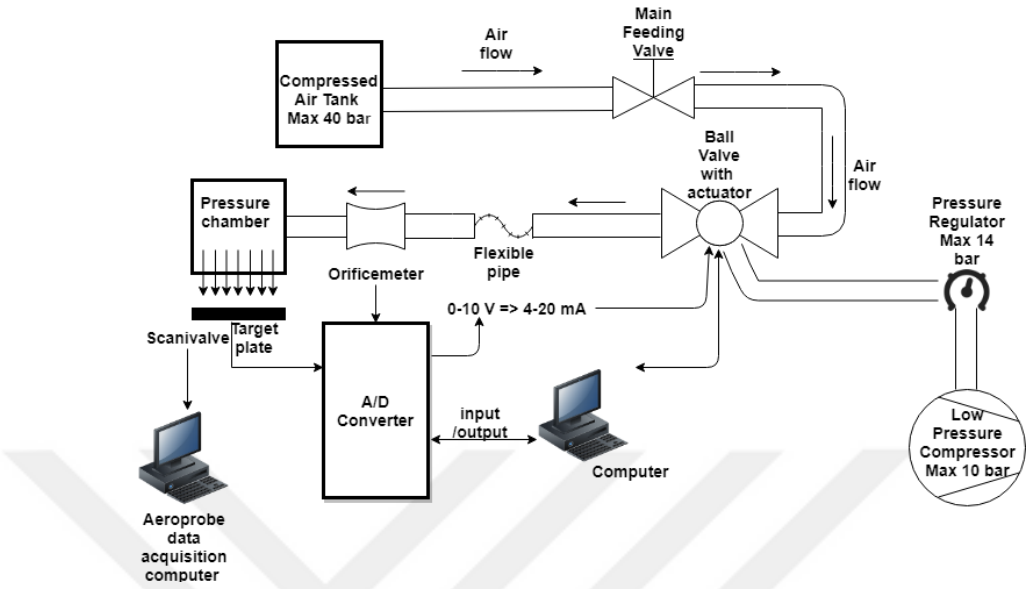

Figure 1.9 Flowchart of the Experimental Set-up

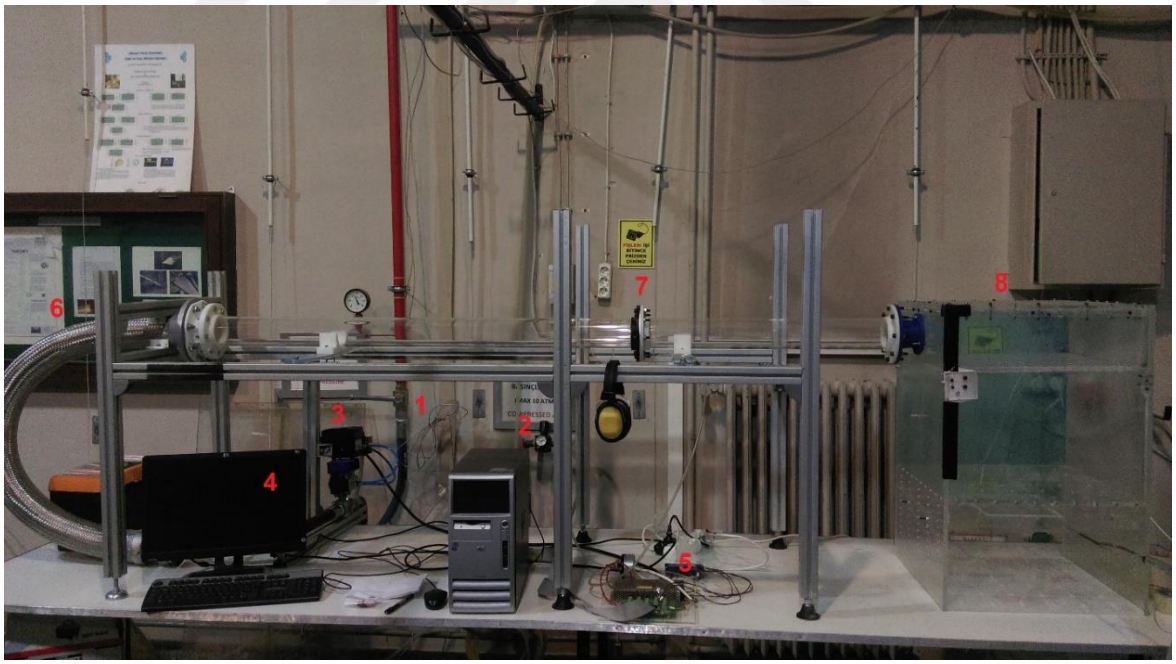

Figure 1.10 Experimental Facility

1) **Manual Main Feeding Valve**
2) **Pressure Regulator (Max 14 bar)**
3) **Ball Valve with actuator**
4) **Computer**
5) **A/D converter and sensor**
6) **Flexible pipe**

7) **Orifice meter**
8) **Pressure chamber**

1.3.1 Orifice meter design and sizing

According to the progress flowchart of the thesis, the work started by writing the proper controlling program for the system. The old set-up was used for that reason and the controlling program was successfully written and tested. The supporting frame and orifice meter sized and manufactured from scratch. An orifice meter is a conduit and a restriction to create a static pressure drop, which allows us to record that pressure drop to calculate the flow rate that passes through the pipe. The orificemeter was designed according to the ISO5167-2:2003 standard. The design of orificemeter starts with selection of the orifice diameter or the beta value, which defines the ratio of orifice diameter to pipe diameter. Most of the literature about the orifice meter covers the beta value from 0.1 to 0.7 range. Low beta ratio means higher-pressure loss, which leads to the higher uncertainty in measurements, which is also applicable when the beta ratio is higher. Therefore, the optimum beta value should be chosen. At the same time, the thickness of the plate should be taken into consideration so that its thickness does not affect the discharge coefficient but thick enough not to be distorted by the forces imposed by the pressure difference. According to the ISO 5167-2:2003, the general requirement for sizing the orifice plate is that the thickness of orifice plate should be in between 0.005D and 0.02D which is roughly in between 0.4 mm and 1.6 mm. The orifice diameter should be greater than or equal to 12.5 mm and the orifice to pipe diameter ratio should be greater than 0.1 but less than 0.75. For this criterion, the pressure taping can be chosen as D to D/2 (**Figure-1.11**). By taking into consideration of these criterions, selection of specifications of orifice plate and meter starts with determining the β or the orifice to pipe diameter ratio.

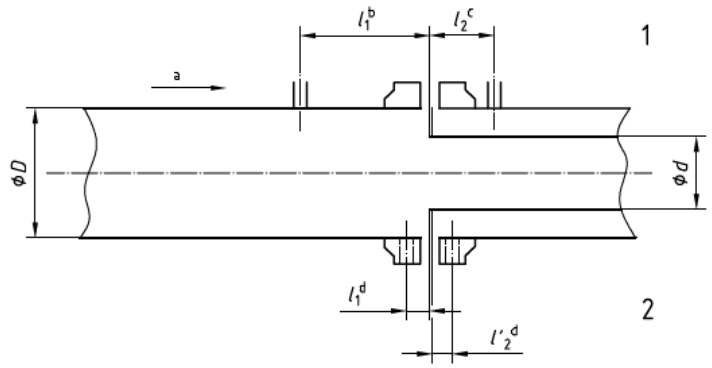

Figure 1.11 Orifice Meter Pressure Taping Configurations (ISO5167-2:2003)

Most of the time β value selection for the orifice plate starts with the educated guess and then iterated with the flow rate equation until the optimum value is reached. It can also be selected going through the similar literature. According to the Flow Measurement Engineering Handbook by Miller (Miller, 1996) it is recommended that for Reynolds number greater than 10,000, it is the best educated guess to choose the β value close to the 0.5. Therefore, the beta ratio for the orifice plate is chosen as 0.5 and the orifice plate thickness was chosen accordingly as 1.5 mm. After selection of the beta value, the discharge coefficient equation was selected according to the ISO5167-2:2003 standard. Selected equation is the Reader-Harris/Gallagher (1998) equation. **Equation-1.1** was fed to the PID controller, which can be found in Control and Data Acquisition part of the thesis.

$$C = 0.5961 + 0.0261\beta^2 - 0.261\beta^8 + 0.000521\left(\frac{10^6\beta}{Re_D}\right)^{0.7} + (0.0188 + 0.0063A)\beta^{3.5}\left(\frac{10^6}{Re_D}\right)^{0.3} + (0.043 + 0.080e^{-10L_1} - 0.123e^{-7L_1})(1 - 0.11A)\frac{\beta^4}{1-\beta^4} - 0.031\left(M'_2 - 8{M'_2}^{1.1}\right)\beta^{1.3} \quad (1.1)$$

$\beta\left(=\frac{d}{D}\right)$: Diameter ratio

Re_D: Reynolds number calculated with respect to D.

$L_1\left(=\frac{l_1}{D}\right)$: Distance of the upstream tapping from the *upstream* face of the plate and the pipe diameter

$L'_2\left(=\frac{l'_2}{D}\right)$: Distance of the downstream tapping from the *downstream* face of the plate and the pipe diameter

For D and D/2 tapping:

$L_1 = 1 \ and \ L'_2 = 0.47$

$$M'_2 = \frac{2L'_2}{1-\beta}$$

$$A = \left(\frac{19000\beta}{Re_D}\right)^{0.8}$$

The desired parameter, mass flow rate, can be calculated by using the **Equation-1.2**, which is also taken from the ISO5167-2:2003 standard.

Flow Rate equation:

$$q_m = \frac{C \cdot \varepsilon}{\sqrt{1-\beta^4}} \frac{\pi \cdot d^2}{4} \sqrt{2 \cdot \Delta p \cdot \rho_1} \quad (1.2)$$

C : discharge coefficient

ε : expansion factor

β : contraction ratio $\beta = \frac{d}{D}$

d : diameter of orifice

D : diameter of duct

Δp : pressure difference at orifice

ρ_1 : flow density before the orifice

The expansibility factor on this equation and for our experimentation was taken also from the ISO5167-2:2003 standard as constant 0.975 due to the experimenting under the Mach 0.3, which is the limit for the incompressibility.

What is more, to avoid the extra device or connection complications, the density was measured first in several flow rates and then from the ideal gas law, density was calculated and fitted to obtain proper variation equation. Then this variation equation was fed to the LabVIEW program to make the density variable with respect to the pressure difference. The fitted graph can be seen in the **Figure-1.12**.

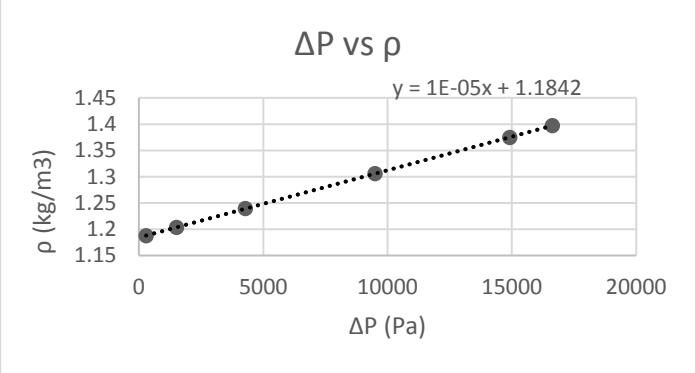

Figure 1.12 Density Variation with Respect to Pressure Difference

After selecting the variables and constants, the next step is to calculate the entrance and exit pipe length and designing the connection flanges. According to the (Çengel & Cimbala, 2013, pp. 351-353), the entrance length can be calculated as follows:

$$\frac{L_{h_{turbulent}}}{D} = 1.359 \cdot (Re)^{1/4} \quad (1.3)$$

$L_{h_{turbulent}}$ = Entrance Length

D = Pipe Diameter

Re = Reynolds Number

Jet Reynolds Number (d = 0.01 m):

$$\mathrm{Re}_{\boldsymbol{d}} = \frac{4 \cdot q_m}{\pi \cdot \mathrm{d} \cdot \mu \cdot \mathrm{n}} \rightarrow \ \mathrm{q}_{\boldsymbol{m}} = \frac{\mathrm{Re}_{\boldsymbol{d}} \cdot \pi \cdot \mathrm{d} \cdot \mu \cdot \mathrm{n}}{4} \tag{1.4}$$

For the at most case, the Re number is taken as 50,000. To ensure for the minimum cases.

$$\mathrm{q}_m = \frac{50{,}000 \cdot \pi \cdot 0.01\, m \ \cdot 1.846 \cdot 10^{-5} (kg \cdot m)/s \cdot 36}{4} \approx 0.26097\ kg/s$$

Reynolds number in the pipe (D = 0.08 m):

$$Re_D = \frac{4 \cdot q_m}{\pi \cdot D \cdot \mu} \tag{1.5}$$

$$Re_D = \frac{4 \cdot q_m}{\pi \cdot D \cdot \mu} = \frac{4 \cdot 0.26097\ kg/s}{\pi \cdot 0.08\, m \ \cdot 1.846 \cdot 10^{-5} (kg \cdot m)/s} \cong 225{,}000$$

Entrance Length:

$$\frac{L_{h_{turbulent}}}{D} = 1.359 \cdot (Re)^{\frac{1}{4}}$$

$$L_{h_{turbulent}} = 1.359 \cdot (225{,}000)^{\frac{1}{4}} \cdot 80\ mm \cong 2367.85\ mm \cong 2.368\ m$$

The exit length, on the other hand, should be shorter than the entrance length (Green & Perry, 2008, p. 6.11). Therefore, foreseen length for the exit is approximately 1 m. However, the calculation considers the air to be taken directly from outside, the bundles or 90^0 turns are not taken into consideration. Therefore, keeping this in mind and referring to the ISO 5167-2:2003 for entrance length with beta value 0.5, the standard gives the entrance length as 22D which can be seen from the **Figure-1.13**, table taken from the ISO 5167-2:2003 standard(ISO 5167-2:2003, p. 16). The entrance length was chosen in between, as 1310 mm and the exit length as 700 mm. For connections of entrance and exit pipes, the flanges were designed according to the DN80 and also between pressure chamber and orifice meter and between flexible pipe and orifice meter, the transition flanges were designed and manufactured by 3D printer. The technical drawings of these flanges can be found in **Appendix A**. The

final part, the pressure chamber is consists of three parts; flow straightener, jet plate and pressure scanner. To analyze wide variety of geometries, the new jet plate designed and manufactured. In new jet plate, the desired geometries are screw fixed to the jet plate to eliminate any gap or flow disruption. In addition to the jet plate, jet geometries also designed and manufactured by 3D printer. Due to the generated rough surface by the 3D printer, in the margin of 0.3 mm error that is generated by printer, these geometries were sandpapered so that the exit surfaces and entrances would be smoother. The two of these jet geometries can be seen in the **Figure-1.14**.

Table 3— Required straight lengths between orifice plates and fittings without flow conditioners

Values expressed as multiples of internal diameter, D

Diameter ratio β	Upstream (inlet) side of orifice plate																				Downstream (outlet) side of the orifice plate	
	Single 90° bend Two 90° bends in any plane ($S > 30D$) [a]		Two 90° bends in the same plane: S-configuration ($30D \geqslant S > 10D$) [a]		Two 90° bends in the same plane: S-configuration ($10D \geqslant S$) [a]		Two 90° bends in perpendicular planes ($30D \geqslant S \geqslant 5D$) [a]		Two 90° bends in perpendicular planes ($5D > S$) [a, b]		Single 90° tee with or without an extension Mitre 90° bend		Single 45° bend Two 45° bends in the same plane: S-configuration ($S \geqslant 2D$) [a]		Concentric reducer $2D$ to D over a length of $1,5D$ to $3D$		Concentric expander $0,5D$ to D over a length of D to $2D$		Full bore ball valve or gate valve fully open		Abrupt symmetrical reduction		Thermometer pocket or well [c] of diameter $\leqslant 0,03D$ [d]		Fittings (columns 2 to 11) and the thermometer pocket	
1	2		3		4		5		6		7		8		9		10		11		12		13		14	
—	A [e]	B [f]	A [e]	B [f]	A [e]	B [f]	A [e]	B [f]	A [e]	B [f]	A [e]	B [f]	A [e]	B [f]	A [e]	B [f]	A [e]	B [f]	A [e]	B [f]	A [e]	B [f]	A [e]	B [f]	A [e]	B [f]
$\leqslant 0,20$	6	3	10	9	10	9	19	18	34	17	3	9	7	9	5	9	6	9	12	6	30	15	5	3	4	2
0,40	16	3	10	9	10	9	44	18	50	25	9	3	30	9	5	9	12	6	12	6	30	15	5	3	6	3
0,50	22	9	18	10	22	10	44	18	75	34	19	9	30	18	8	5	20	9	12	6	30	15	5	3	6	3
0,60	42	13	30	18	42	18	44	18	65 [h]	25	29	18	30	18	9	5	26	11	14	7	30	15	5	3	7	3,5
0,67	44	20	44	18	44	20	44	20	60	18	36	18	44	18	12	6	28	14	18	9	30	15	5	3	7	3,5
0,75	44	20	44	18	44	22	44	20	75	18	44	18	44	18	13	8	36	18	24	12	30	15	5	3	8	4

NOTE 1 The minimum straight lengths required are the lengths between various fittings located upstream or downstream of the orifice plate and the orifice plate itself. Straight lengths shall be measured from the downstream end of the curved portion of the nearest (or only) bend or of the tee or the downstream end of the curved or conical portion of the reducer or the expander.

NOTE 2 Most of the bends on which the lengths in this table are based had a radius of curvature equal to $1,5D$.

a S is the separation between the two bends measured from the downstream end of the curved portion of the upstream bend to the upstream end of the curved portion of the downstream bend.

b This is not a good upstream installation; a flow conditioner should be used where possible.

c The installation of thermometer pockets or wells will not alter the required minimum upstream straight lengths for the other fittings.

d A thermometer pocket or well of diameter between $0,03D$ and $0,13D$ may be installed provided that the values in Columns A and B are increased to 20 and 10 respectively. Such an installation is not, however, recommended.

e Column A for each fitting gives lengths corresponding to "zero additional uncertainty" values (see 6.2.3).

f Column B for each fitting gives lengths corresponding to "0,5 % additional uncertainty" values (see 6.2.4).

g The straight length in Column A gives zero additional uncertainty; data are not available for shorter straight lengths which could be used to give the required straight lengths for Column B.

h $95D$ is required for $Re_D > 2 \times 10^6$ if $S < 2D$.

Figure 1.13 Entrance length table according to the ISO 5167-2:2003

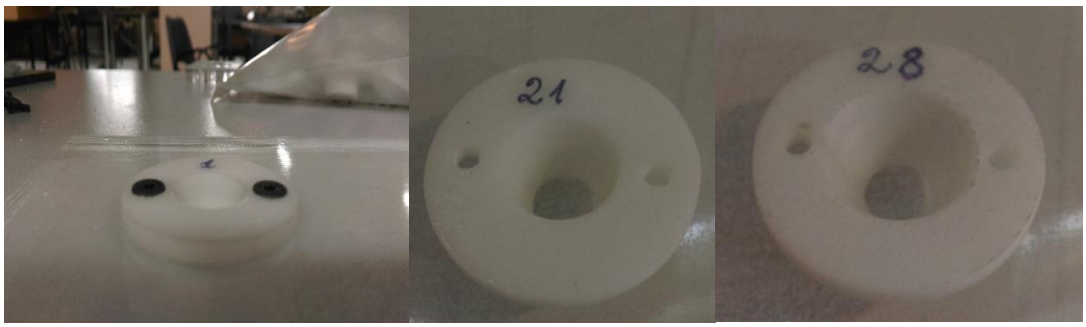

Figure 1.14 Manufactured Jet Geometries

Jet plate as seen in the **Figure-1.15** was manufactured from Acrylic plate by the Laser cut facility provided by the Trisonic Research Laboratory within the Istanbul Technical University.

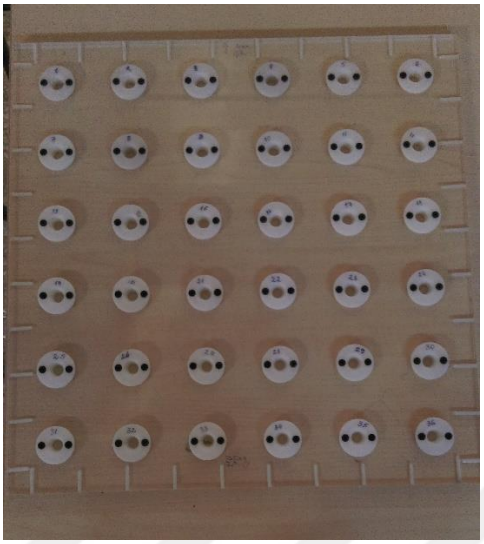

Figure 1.15 Jet Plate with 300 nozzles

The proper pressure scanner was also designed and manufactured so that all of the jet plate can be scanned. The pressure scanner is consist of four parts which are the local or small rotatable scanner (300 mm x 300 mm) with 328 socket holes so that in one scan four impingement zone can be scanned, the global rotatable pad (500 mm x 500 mm), 2 mm fillets for altering the scanning interval and two 10 mm side parts to eliminate the gaps in the front and back part of the pressure chamber (**Figure – 1.16**).

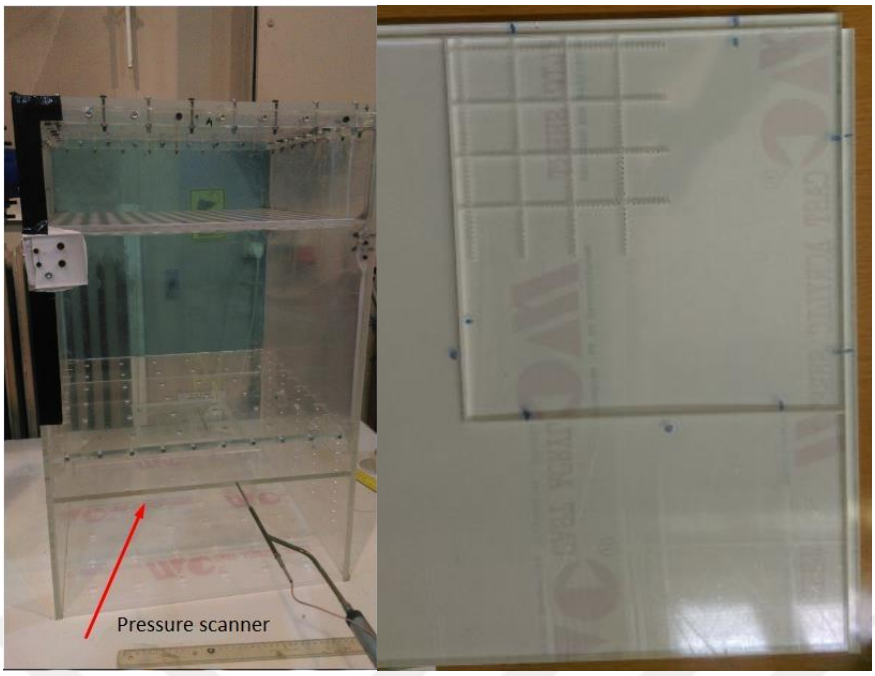

Figure 1.16 Pressure Chamber and Pressure Scanner

1.3.2 Hot-wire anemometry

Hot-wire anemometers are devices that helps to measure the variations in turbulent flow such as mean and fluctuating-velocity components, mean and fluctuating temperature, etc. The probe consists of two parts. The first part is both extender and connection between the data acquisition system. The second part is the wire or filament extended between the two ends of the fork-like part. This filament is commonly made of tungsten, platinum and platinum-iridium. The sensor either operates in constant current or constant temperature configurations. In constant current configuration, it is possible that the probe can burn out due to lack of cooling air. Similarly, if the flow is too low, it can lead to the insufficient heating of sensor and results in getting low quality data. Therefore, the mostly used sensor configuration is constant temperature and in our case the sensor is constant temperature hot-wire anemometer. The working principle of sensor relies on the fact that the electrical resistance of a metal conductor is a function of its temperature. The supplied electric current heats up the filament, which is disrupted with the fluid flow typically airflow. The airflow reduces or causes the fluctuation in temperature, this reduction in temperature is recorded, and by using the energy balance equation, the mean and fluctuation velocity is calculated (**Figure – 1.17**).

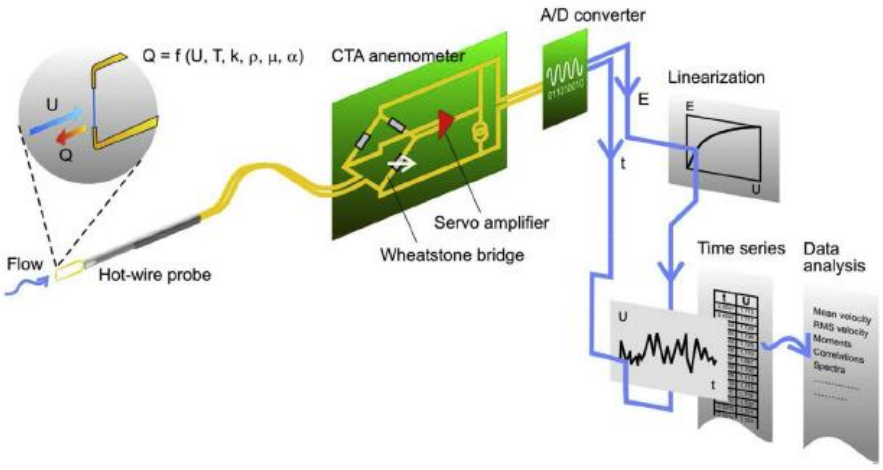

Figure 1.17 Complete schematic of constant temperature anemometer (courtesy of Dantec Dynamics)

Depending on the usage, there are several categories of probes. In the simplest case, there is a thin wire suspended between two prongs or a thin metal film deposited on an electrically insulating substrate. The first case is mostly used in gaseous or non-conducting liquid environments. Whereas, film sensors are designed to use in water and conducting liquids. Additionally, these probes also comes with different configurations of prongs or substrates like one or multiple wired configurations. In our experimentations, miniature wire probe which is designed for usage in boundary layers (**Figure – 1.18**).

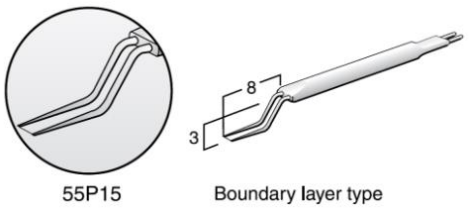

Figure 1.18 Boundary Layer Type Probe drawing (courtesy of Dantec Dynamics)

The probe that was used in the experiments can be seen in the **Figure – 1.19**.

Figure 1.19 Boundary Layer Probe

The whole system of the hot wire anemometer consists of five parts which are Dantec Dynamics Traverse system, Streamline System of anemometer or the main system, probe calibrator, NI CA-1000 signal conditioner, and computer (**Figure – 1.20**). There is also a supporting part which provides the support to the probe on the traverse system. To fix the probe supporting tube to the traverse, new fixing part was designed by 3D printer so that the supporting part would hold the probe tube in constant position or preventing any deviation from desired position. Technical drawing of supporting part can be found in **Appendix-A**.

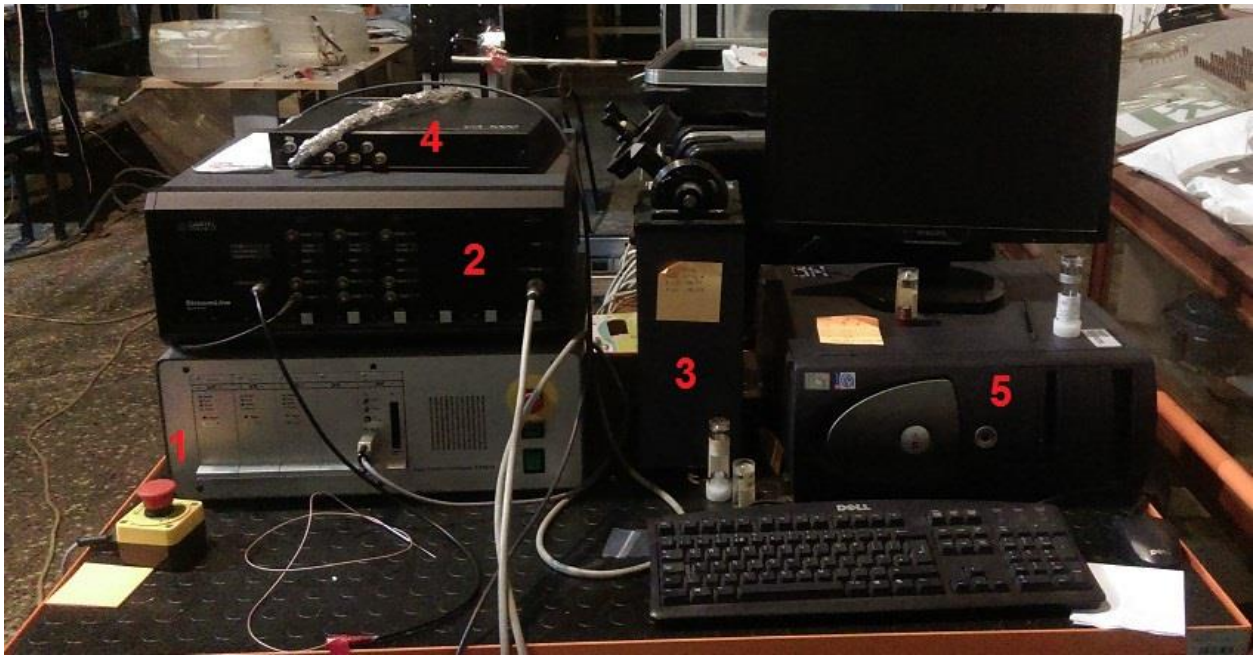

Figure 1.20 Hot-wire Data Acquisition System

1) Traverse system controller

2) Main system of hot wire anemometer

3) Hot wire calibrator

4) National Instrument CA-1000 signal conditioner

5) Controlling and visualizing computer

1.3.3 Aeroprobe system

Aeroprobe is another system that was used in experiments. The main purpose of this system is to record the pressure difference coming from the pressure scanner of pressure systems device and the pressure scanner that was designed and manufactured by using the laser cutter that was provided by Trisonic Laboratory. The pressure differences were recorded to scan the whole area of the jet plate. The Aeroprobe system is shown in the **Figure-1.21**.

Figure 1.21 Aeroprobe System

1) **Aeroprobe data acquisition system.**
2) **Computer for visualization of data.**

Additionally, in between the Plexiglas pressure scanner and the aeroprobe system, there is a multiple pressure scanner probe which have 32 channels to obtain the 32 pressure readings. This probe can be seen in **Figure-1.22**.

Figure 1.22 Pressure Scanner

To calibrate the scanner and check the 32 channels, the calibration device was designed and manufactured. The main purpose of this calibration device is to detect or check the operational condition of each and every channel. Therefore, small pressure chamber was designed to lead all the flow to that chamber so that all the channels would read the same pressure difference. The channel that largely deviates from the constant pressure difference was marked to get the data accordingly. The calibration and data showed that the only deviated channel is the 22nd channel on the pressure scanner. The calibration device can be seen in **Figure-1.23**.

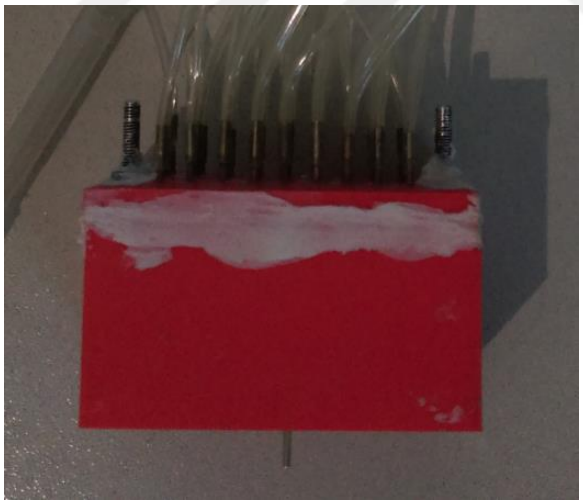

Figure 1.23 Calibration Device for Pressure Scanner

1.4 Literature Review

Jet impingement cooling is an attractive cooling technique which is used in many industrial applications like turbine cooling. To illustrate, the annealingof metal, the tempering of glass sheets, the cooling of turbine blades, the chemical vapor deposition,

propulsion jetto-flaps interaction in STOL aircraft and thermal anti-icing systems of wings(Bu et al). The key parameters that affect the heat transfer performance of a single impinging air jet are Reynolds number,Prandtl number, jet diameter, jet-to-target spacing, confinement and nozzle geometry. There are countless experimental and numerical works which investigated the effect of these parameters on impingement jets.

The paper (Jennerjohn et al.) deals with the array of impinging jets for the cooling purposes. The parameters that are taken into consideration are hole array spacing, jet-to-target plate distance, and Reynolds number. The cooling air directed to the target plate with array of jets that extracted to one direction in the channel, the other three sides were bounded. The range of Reynolds number that was considered for the experiment was from 8,000 to 50,000 and jet-to-target distances were 1.5D, 3.0D, 5.0D, and 8.0D and finally for streamwise and spanwise hole spacing 5D, 8D, and 12D were considered. Experiments revealed that the local Nusselt numbers increase at each x/D or non-dimensional streamwise coordinate, as the Reynolds number increases and as the hole spacing X/D = Y/D decreases. The results showed that the maximum Nusselt number was obtained in the case of Z/D of three and the jet Reynolds numbers 8200, 20,000, and 30,000. In addition, the maximum Nusselt number was also obtained in the case where jet Reynolds number is 52,000 and jet-to-target distance is either 1.5, 3.0, or 5.0, depending on the magnitudes of hole spacing, both streamwise and spanwise and also streamwise locations x/D. Examining the results revealed that as the normalized jet-to-target distance increases in a certain Reynolds number, the maximum Nusselt number tends to shift to the larger x/D locations. This is implication of the large advection distances between the impingement hole exits and the target plate. What is more, the variations of the Nusselt number is also believed to be the production of two phenomena which are the coherence of individual jets and the strength of adjacent shear layers and the development and advection of vortices generated by Kelvin-Helmholtz instabilities. The deduced overall results from the experimental work is that there exist a complex dependence of local Nusselt numbers on the hole array spacing, jet-to-target plate distance, and impingement jet Reynolds number.

The experimental study by Weihong Li et al. investigated the effects of varied Reynolds number, hole spacing, jet-to-target distance and hole inclination on heat transfer by impinging jet. The experiments were conducted with the following

different variables: streamwise and spanwise jet-to-jet spacing (X/D, Y/D)4~8, jet-to-target distance (Z/D) 0.75~3 and finally the Reynolds number variations are between 5,000 and 25,000. In addition to previous properties, hole inclination (θ:0° ~ 40°) pointing to the upstream direction was analyzed for the sake of comparison with normal impinging jet case. The experiment was done by transient liquid crystal technique to measure heat transfer coefficients. The experimental study concentrated on the obtaining the highly resolved heat transfer coefficient distributions on the target plate in range of Reynolds number and also the correlation was made between Reynolds number and impingement geometrical parameters to obtain two-regime new coefficients for the Florschuetz's correlation. The main outcomes of the study was that the discharge coefficients are increased by increasing the cross areas and also the same happened as the Reynolds number was increased, it was observed that the coefficient was mostly run around 0.6 and 0.75 for channel cross areas of py×pz=3 and 18. In addition, the experiment showed that the surface heat transfer and Nusselt number was mostly affected by the hole staggering parameter, the x and y directional distances between holes. It is observed that higher values of dx and dy leads to the decrease in the heat transfer because of the insufficient coolant coverage in the area. For the surface Nusselt number, it was observed that for the large stream wise jet-to-target distance, the surface Nusselt number decreases and increases as the distance reduced. Finally, the impingement inclination, the experiments showed that there is no significant effect of this parameter on the averaged-Nusselt number, only slight change was observed for the local heat transfer distribution.

This paper is the follow up work of the previous experimental work, dealing with the array of jets. Different from the previous paper Weihong Li et al. is trying to analyze and optimize the effect of the different Reynolds number, hole array patterns, jet-to-target spacing and hole inclination on convective heat transfer and minimize the amount of cooling air. As an indicator and measure of convective heat transfer, spatially resolved target surface heat transfer coefficient distribution was considered and were measured by using transient liquid crystal (TLC) measurement technique. The considered range of Reynolds number is 5,000 to 25,000. Streamwise and spanwise jet-to jet spacing X/D, Y/D is 4 – 8 and the experimented jet-to-target spacing (Z/D) range is 0.75 – 3. In addition, to these properties, the effect of hole inclination (θ: 0 – 40^0) is investigated. The new correlation coefficient was obtained for Florschuetz's also by correlating geometrical properties and Reynolds number.In

terms of discharge coefficient, the experiments showed that as the Reynolds number increases, there is a slight effect on the discharge coefficient. Furthermore, it is observed that when the Re number kept in the fixed number, as the channel cross-area increases, discharge coefficient enhanced. This is an indication of that low channel cross-area causes high flow friction. Overall effect of the Reynolds number on Nusselt number is as expected. As the Reynolds number increases, the Nusselt number increased. Evaluating the effect from quantitative point of view, Nu number increased by a factor of 3.5 as the Re number increased from 5,000 to 25,000.Considering the jet-to-jet spacing, the experiments showed that the hole pattern in x and y directions are highly associated with the coolant coverage or the hole density. The results showed that larger values of dx and dy lead to the reduced heat transfer performance due to the low coolant coverage of the jet holes. The interaction between adjacent jets was maintained for px=4 and py=6 but for px=8, jets disconnect and form a circular shape. For the jet-to-target spacing variation, the experimental work revealed that as the spacing between impinging jet and target decreases, it generates accumulation of the crossflow in the downstream which lead to increase of momentum and as a result an overall shift of jet core and intensification of heat transfer coefficients. However, for the case when the jet-to-target spacing is high, the heat transfer patterns are quite circular and for pz = 3, the spatial redistribution of the horseshoe vortex pattern associated with downstream jets are less pronounced. As a result, the overall observation showed that the heat transfer level of pz = 0.75 and 1.2 is higher than that of pz = 2 and 3. In addition, regarding to the effect of the hole inclination to the heat transfer, it was observed that the increase in the inclination of hole changes the heat transfer patterns from circular to an ellipse shape. As the inclination angles increased from 00 to 200, the Nusselt number reaches to the peak value at 20 but it decreases when the inclination become 400 due to increased impingement distance. In spite of the increase in local heat transfer pattern in different angles, the obtained data showed that the deviations of area-averaged Nusselt number of normal impingement and inclined impingement are small in terms of standard error. This illustrates that the inclination of impinging jet hole exerts no influence on the area averaged Nusselt number.According to the optimization of coolant consumption, experimental work demonstrated that designers should put more effort on impingement configuration with larger py and smaller px if non-dimensional area is fixed.

The experimental study by Czeslaw et. al. concentrated on the visualization of the near-field flows of natural free and impinging round jets. The study was done by using the smoke-wire flow visualization technique. The study divided the observation into two categories, which are free round natural jet, and round impinging jet. In the first case, the free round jet, submerged into a laboratory space where airflow is generated by the simple subsonic jet rig. The main consideration was put, to investigate how the regular vortex structures are initiated and developed in the developing (transitional) region. The pictures were taken at higher jet Reynolds numbers, beyond approximately 20,000 or U_0=6 m/s. Due to the cyclic thinning and thickening of the smoke filaments, which gives rise to the Karman vortex shedding. In addition, starting from the source, mouth of the nozzle, and the successive stages of the vortex formation was observed and observations showed that the flow of air starts with the case where the flow is starting to become turbulent and the nozzle is surrounded by a thin laminar unstable laminar shear layer. This laminar shear layer exhibits all the features of Kelvin-Helmholtz instability. This instability give rise to the new structure which arise from the a small lump of vorticity-containing fluid, separating from top crest of sinusoidal wave and convecting downstream as starts to roll up and develop in size and strength to form the toroidal vortex. The observation revealed that if the toroidal vortex generation is triggered too early, by background large-scale turbulence peak or by some internal disturbances or external acoustic excitation, the vortex become weaker and is usually very soon engulfed by the earlier formed large vortex. As the characteristic length near the nozzle, the momentum thickness is taken but beyond a distance of about 1.5D, the toroidal vortex grows in scale to become comparable with nozzle radius, makes the passing frequency of large toroidal vortices become lower. Additionally, the entrainment of the free jet to the surrounding fresh fluid has a significant effect on jet characteristics. Previously mentioned toroidal vortex also affected by mixing which does not change significantly the main diameter but strongly contracts the jet core and stretches fluid elements along the jet axis. The other analyzed jet type is the round impinging jet where nozzle-to-plate separation of 1.2, 2-4 was taken to observe how the low nozzle-to-plate separation affects the flow at the plate surface in the impinging region. For the spacing 1.2, it was observed that the large-scale toroidal vortices develop in the mixing region and interact with the plate reaching the plate at a radius of r/d = 0.7 – 0.9. As the distance gets lower, the vortex stretches increasing its diameter. During observation, among the stretched vortices, some dark

triangular spots containing fluid drawn from the stagnation point vicinity and also ring-shaped wall eddies were visible due to induced by the large-scale toroidal vortices, stretched and diverged in the radial direction. At the end within the range of radius r/d = 1 – 2, toroidal vortices and wall eddies were abruptly merged in the transition region and transformed into a developed radial wall jet. Overall, the main aim of the study was to illustrate the behavior of natural free and impinging round jet at low nozzle-to-plate separations.

The experimental work by Park et al. investigated the effect of variable Reynolds and Mach number. In addition to these variations, the diameter of the jets were also varied. The variations were analyzed individually. In other words, for the constant Mach number, the Reynolds number was variable and vice versa. The considered Reynolds numbers were in between 30,000 to 60,000 and the interval of Mach number was between 0.1 to 0.6. The diameter of the jet was also a variable, which affects the thickness of the jet plate that was taken as 1D. The total number of the experiments that was conducted was 20. The heat transfer rate evaluated by infrared camera. The main parameters that aimed to determine, were impingement hole discharge coefficient, Nusselt number variations with Reynolds number and Nusselt number variations with Mach number. For the discharge coefficient, the case where Reynolds number was constant, 30,000, as the impingement Mach number increases, the discharge coefficients decreases. The same trend is applicable for the opposite version of the experiment, where the Mach number is 0.2 and Reynolds numbers varies. The constant Reynolds number data generally lie below the constant Mach number data. For the case where the Mach number kept constant at 0.2 and the Reynolds numbers were varied from 11,000 to 59,700, the general trend suggested that as the Reynolds number of jets in streamwise direction increases, substantially the Nusselt number increases. The specific streamwise and spanwise variations were x/D = 32, 48 and y/D = 8, 0 . Smaller peak values of Nusselt numbers were observed at x/D = 32 and 48. Regarding to the Nusselt number variations with Mach number, the experiment conducted for constant Reynolds number of 30,000 and for variable Mach number 0.2, 0.45, and 0.6. In this case, the constant spanwise location or y/D = 8 was considered and the plot was created for variation of Nusselt number with x/D location. The same trend was observed here also, overall, Nusselt number increased as the jet Mach number increases. Additionally, the smaller peaks were observed in x/D = 32 and 48

locations which evidently due to the local Nusselt number increase at spanwise locations approximately halfway between the impact points of nearby impinging jets. Goodro et al. experimentally investigated the effect of the Mach number, Reynolds number and hole spacing on heat transfer or the surface Nusselt number. The investigated jet type was the array of jets that were assigned from the constant circular geometry. Jet-to-target spacing was equal to 3D and the thickness of the jet plate was 1D. The one of the main variable properties of the investigation is the Reynolds numbers, which was taken in between 17,300 to 60,000. Jet spacing was the other parameter, which were 5D, 8D and 12D, in streamwise and spanwise directions. The variation interval of the Mach number was in between 0.1 to 0.45, which also allowed to take into consideration the compressible situation. In addition to these parameters, the results were compared with results and correlation from Florschuetz et al., concerning to the hole spacing. Both local spatially resolved and averaged Nusselt numbers were measured by the help of infrared thermography and energy balance techniques. The results obtained from the experiments based on the comparison of the several nondimensionalized physical properties. The crossflow mass velocity-to-jet mass velocity ratio is the one of them. The investigation showed this ratio was lower in the case when the hole spacing is the largest, 12D but as the spacing gets smaller, the ratio becomes larger. Another parameter is the discharge coefficients which represent average values for all of the jet holes on a particular test plate. The obtained data and graphs showed that when the Mach number (0.2) and holes spacing kept constant, the discharge coefficient decreases with increasing the Reynolds number. The experimental investigation also analyzed the variation of spatially resolved local Nusselt numbers with Reynolds number, keeping the Mach number constant as 0.2. In this comparison, three different holes spacing were taken into consideration, these hole spacings were 5D, 8D, and 12D. The Reynolds numbers that were takin into consideration were Rej = 17,300, 30,000 – 30,500, and 60,000. The paper presented thermographic results, which showed that due to the spent air crossflow and the cumulative effects of the jet interaction, the local Nusselt number decreases regardless of Reynolds number with every x/D from hole spacing 8D to 12D, this reduction was more pronounced with 5D. The results were also presented for the case of different hole Reynolds numbers at constant Mach number for each of hole spacings. For this case, the obvious increase in the Nusselt numbers with the increase of the Reynolds number were observable from the presented data. Another case for comparison was

variations of spatially resolved local Nusselt number when the Reynolds number is constant Rej = 30,000 – 30,500 and the Mach number varies from 0.09 to 0.45. Specifically, Mach numbers of 0.09, 0.17, 0.30, and 0.38 for hole spacing 5D; Mach numbers of 0.20, 0.35, and 0.45 for hole spacing 8D; and finally, Mach numbers of 0.10, 0.17, 0.38, and 0.45 for hole spacing 12D. This comparison showed that there was a decreasing trend in local Nusselt number with increasing x/D, the greatest decrease occurred in hole spacing of 5D. This reduction was considered to be the result of increasing amounts of spent air crossflow with decreasing hole spacing. In addition, the overall results showed that the local Nusselt number increases with increasing the Mach number which considered to be the effects of compressibility on the vortices and associated vortex structures that form around each impingement jet. Line averaged Nusselt numbers were also analyzed and graphed, the averaging was taken over y/D from -2.5 to +2.5 for hole spacing of 5D, over -4.0 to +4.0 for hole spacing of 8D and over -6.0 to +6.0 for hole spacing of 12D. This analysis for variable Reyolds number and constant Mach number, showed an increasing trend with the increase of Reynods number. The same trend was observed for the opposite case where the Mach numbers varied and the Reynolds number kept constant. This trend was again considered to be the result of the increased spent air crossflow. In addition, the spatially averaged Nusselt numbers measured for three different hole spacing and compared with values from Florschuetz et al.. The comparison was carried similar to the previous cases where the Reynolds numbers varied and Mach number was kept constant and visa verse. For the first case the data shows good agreement with the Florschuetz et al. but in the second case, for specific incompressible Mach numbers the spatially averaged Nusselt numbers are in agreement with each other but higher than the values of Florchuetz et al. which was considered to be result of bigger hole spacing, were not considered in the Florchuetz et al. work. Finally, since the Mach numbers pass the compressibility range, the effect of compressibility on area averaged Nusselt number was also analyzed. The cumulative results showed that as the jets get closer, both line and area averaged Nusselt numbers increases. This behavior of the jet was considered to be the result of the interaction of the neighbor impingement jets which interact with each other with generated unsteady vortex and votex rings. The competition between these vortices determine the local stagnation temperature distribution and static temperature distributions on the impingement target plate. The slight difference in

compressibility alters these complex vortex structures and also responsible for enhancing the surface heat transfer.

Heat transfer characteristics were measured by Metzger et. al. for two dimensional arrays of jets impinging on a surface parallel to the jet orifice plate. The effecting parameters that were analyzed were chordwise jet hole spacing of 5 and 10 hole diameters, spanwise spacing of 4 to 8 diameters, channel heights from 1 to 3 diameters with some data at 6 and finally mean jet Reynolds number from 5 to 20,000. For different combinations both inline and staggered hole pattern were used. The graphs were presented as the relation between Nusselt number and geometric parameters which are channel height (z/d), chordwise (xn/d) and spanwise (yn/d) hole spacings and hole pattern (inline and staggered). The analysis was made in four different size configuration of experimental set-up. These configurations differ from each other by interchangeable plenum size, which differ the chordwise length and the channel length. These configurations were symbolized by letters which are A, B, C, and D. The chord length of A configuration is 6.35, B configuration 12.7 cm, C configuration 25.4 cm, and D configuration 38.1 cm. The maximum possible resolution ranges from 2xn for the A size to xn/3 for the D size. The results in terms of Nusselt number were categorized in three ways, which are (1) mean values, Nu, averaged over the entire active heat transfer surface, (2) low-resolution values averaged over xn or 2xn, (3) higher-resolution values averaged over xn/3 or xn/2. The experimental results showed that the channel height has a little effect on Mean Nusselt number. Furthermore, during the experiments, the A-size configuration has a significant compressibility flow characteristics to increase the flow Reynolds number, which was obtained because of large pressure drops. However, in the real case scenario, the pressure levels in turbine applications are higher with correspondingly lower Mach number. Therefore, the model that is larger than the A-size best models the prototype heat transfer characteristics for the gas turbine engine application. The results also showed that there is only a slight effect of channel height on the mean Nusselt number. In the case of low-resolution chordwise profiles, the different set of streamwise and spanwise cases were graphed and the results showed that for every set (xn/d, yn/d) and the channel height $1 \leq z/d \leq 3$, higher the channel height, greater the cooling rate. At the same time, as the flow goes downstream, the opposite is true, smaller values of z/d, give higher cooling rates. This effect is related to the channel height, where this range of channel heights creates minimal crossflow, which is the upstream condition, increases with z/d,

while cooling rates due to channel-type flows, which here arise downstream and vary inversely with channel height. The comparison of the inline and staggered hole patterns showed that mean heat transfer coefficients for every case were larger in inline pattern than those for the corresponding staggered patterns. The difference become the largest for the highest hole density (xn/d = 5 and yn/d = 4) and the largest channel height (z/d = 2 and 3). It was considered reasonable result because at the downstream location presumably interacted jets enhances the heat transfer. Finally, the high-resolution data was taken and analyzed for the limited geometric characteristics. The periodic variation of the Nusselt number was observed for streamwise and spanwise hole spacings of 10 and 4 and the channel height of 2. The additional channel heights, hole spacings and flow rates is currently underway and will be reported in the subsequent paper.

2. CONTROL

2.1 Flow Control and Data Acquisition (LabVIEW)

For the most of the experimental and industrial works, there is always a need to control the certain parameters in order to conduct controlled experiment. Controlled experiment is the scientific test that is aimed to prove the hypothesis by doing a test under controlled conditions. Controlled condition is the case where conductor of the experiment keeps one or few parameters changed with time while all the others kept constant.

In our case, the flow rate of air was kept constant by using the LabVIEW (Laboratory Virtual Instrument Engineering Workbench) which is a system-design platform and development environment for a visual programming language from National Instruments. By the help of DAQ assistant, that transfers the obtained analog or the voltage values to the LabVIEW environment where the obtained voltage value calibrated and converted into the more meaningful parameters like pressure, pressure difference, temperature, etc. Desired conversion in this case is pressure difference, which was converted into flow rate by series of equations.

The logical control of the flow rate was done by the LabVIEW built-in toolkit PID. PID control is the commonly used tool in scientific experiments and industrial machines. PID controller stands for the Proportional-Integral-Derivative controller. The basic idea behind the PID is that the overall loop is trying to reach to the intended set point, given by the controller. The set point is reached by calculating the error between set point and calculated value. If the set point was not obtained, then the iteration proceed with calculation of Proportional-Integral-Derivative coefficients where the iteration continue until the set point is reached. The general mathematical representation of the PID controller is as follows:

$$u = K_p e + K_I \int e dt + K_d \frac{de}{dt} \tag{2.1}$$

Above equation can be represented in terms of block diagram (**Figure – 2.1**):

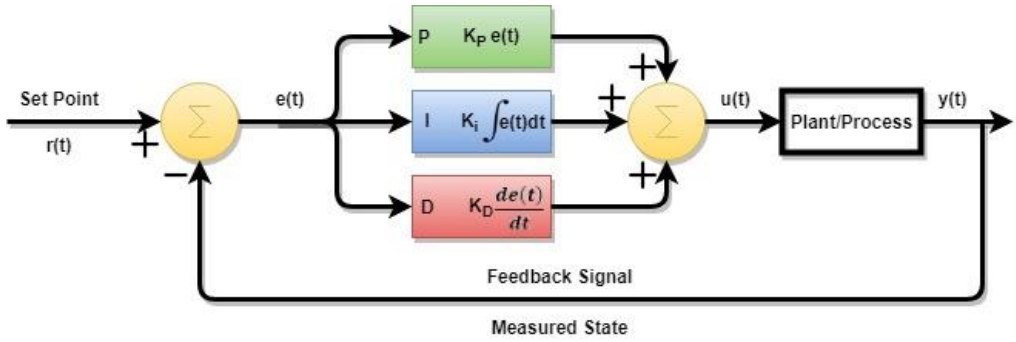

Figure 2.1 Block Diagram of PID Control

Transfer function for the above block diagram:

$$K_p + \frac{K_I}{s} + K_D s = \frac{K_D s^2 + K_P s + K_I}{s} \tag{2.2}$$

The tuning or determining the coefficients, is an important part of PID control. The main objective of tuning is to get from system both fast responses and good stability. However, it is difficult to get both at the same time in the first attempt. The common methods to find the tuning parameters is through the use of tuning rules or methods. The methods are also classified into two main categories. They are simply open and closed loop methods. There are several known closed and open loop methods for tuning which are Ziegler-Nichols method for closed loop method, Tyreus-Luyben method and Cohen and Coon method for open loop etc. (Haugen, 2004). Besides these open and closed loop methods, parameters can be found by experiments. Additionally, intuitive P-I-D method also used during the experiments (Haugen,2004). For finding the K_p value, the assumption of P-I-D method is used and keeping the other parameters in a certain value, K_p = 1 was tried and decreased %20 until the response or the disturbance occurred. The first effective proportional parameter was 0.1. Then with the similar method, other parameters modified and stability was obtained with K_p = 0.1, K_I = 0.01 and K_D = 0.05. However, during the experiments, it was observed that the response of the control system to the big changes of set point value triggers many oscillations, which can be recovered in a long period. Therefore, with the same logic of P-I-D method, K_p decreased and more stable but slow converging range was found. This observation allowed us to use variable K_p value. The process starts with 0.01 and as soon as the system finds a stable range, it is changed to 0.1 to increase the

convergence. These parameters allows us to control the flow rate with the error of 0.02%.

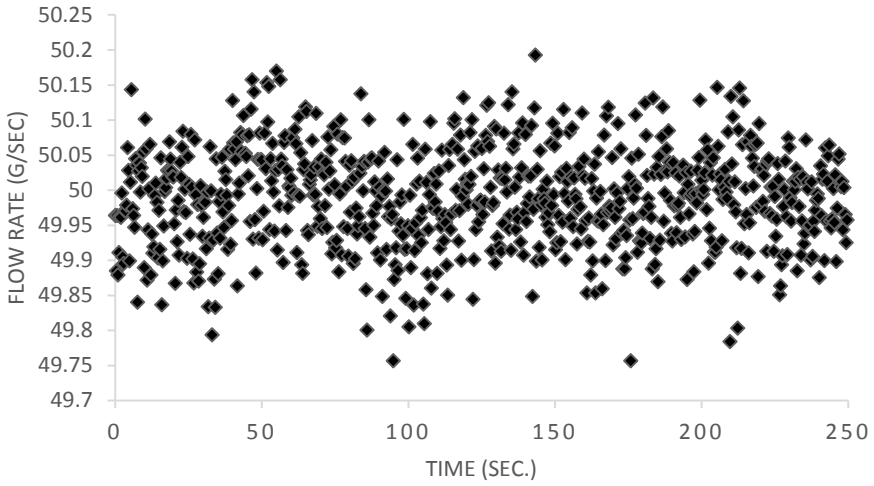

Figure 2.2 PID Controlled Flow Rate versus time

The process starts with feeding data to the calibration equation of pressure transducer in the LabVIEW, with the **Equation – 2.3** and then it is converted to the pressure difference by multiplying to the gravitational constant.

Calibration equation:

$$y = 702.36 \cdot x - 19 \tag{2.3}$$

Process continues with obtaining the flowrate, which requires several constants, and the quantity that is obtained by iteration. The constants that are used in the process are diameters ratio, which is also called beta value and expansibility factor.

After defining the parameters, the flow rate is calculated by the **Equation - 2**, which is mentioned in **1.3 Experimental set-up** part of the thesis.

Calculation of the flow rate allows us to derive and obtain several parameters, which are Reynolds number and Mach number. Parameters are described with the equations as follows:

Reynolds number: Equation – 1.4

Mach number:

$$U = \frac{Re_D \cdot \mu}{\rho \cdot D} \quad and \quad Ma = \frac{U}{a}, \quad a = \sqrt{\gamma \cdot R \cdot T} \tag{2.3}$$

The only quantity that is found by iteration is the discharge coefficient. The iterative process for the discharge coefficient starts with the initializing with any value, in this

case, it is 0.1, further calculation of the Reynolds number from the flowrate updates the discharge coefficient, and by reducing the error between old value and new value to the 0.01, the discharge coefficient is obtained and used in the flowrate. PID controller follows this process and iterates according to the given set point. Since the experimenting Mach number is in the incompressible range, the Reader-Harris/Gallagher (1998) equation (**Equation – 1.1**) was used for calculation of discharge coefficient. The iterative sequence for calculation of discharge coefficient is shown below.

1) Initialization of discharge coefficient C by giving arbitrary value.

2) Calculation of flow rate q_m by using present value of discharge coefficient

3) Determination of Reynolds number by using the calculated value of flow rate

4) Finding Reynolds number allows us to find new value for discharge coefficient

5) Comparison of present and old arbitrary value of discharge coefficient. If the error:

$$\left|C_{present} - C_{old}\right| \leq 0.001 \tag{2.4}$$

Then continue to the calculation of the flow rate with present value of discharge coefficient and continue to the PID controller. Otherwise, go back and plug calculated discharge coefficient and do all the previous steps again.

2.2 Uncertainty Analysis

Uncertainty analysis helps us to determine the uncertainty in the experimental measurments. Because, during the exepriments one can deal with several devices which have certain precision and that may affect the measured parameter. Therefore to calculate the total uncertainty, the unceratinty of individual parameters are calculated and summed up at the end. This is called Kline and McClintok method.

$$w_R = \left[\left(\frac{\partial R}{\partial x_1} w_1\right)^2 + \left(\frac{\partial R}{\partial x_2} w_2\right)^2 + \cdots + \left(\frac{\partial R}{\partial x_n} w_n\right)^2\right]^{1/2} \tag{2.5}$$

Flow rate equation: **Equation – 1.2**

The uncertainities of measurement devices are known from the documents that are provided by the manufacturing company. The overall uncertainities of parameters are shown below.

Table 2.1 Uncertaint values of measurment devices

Measurment System	Parameter	Unit	Uncertainty
Pressure Scanner	Pressure	Pa	Full Scale ±0.05 %
Thermocouple	Temperature	^{0}C	0-100 ^{0}C 1.1 %
Pressure Sensor	Pressure difference	Pa	Full Scale ±0.15 %

Uncertainty due to pressure difference Δp

$$\frac{\partial q_m}{\partial \Delta p} = \frac{C \cdot \varepsilon}{\sqrt{1-\beta^4}} \cdot \frac{\pi \cdot d^2}{4} \cdot \frac{2}{2}(2 \cdot \Delta p \cdot \rho_1)^{-\frac{1}{2}} = \frac{C \cdot \varepsilon}{\sqrt{1-\beta^4}} \cdot \frac{\pi \cdot d^2}{4} \cdot \frac{1}{\sqrt{2 \cdot \Delta p \cdot \rho_1}}$$

$$= \frac{\boldsymbol{C \cdot \varepsilon}}{\sqrt{\boldsymbol{\rho_1 \cdot (1-\beta^4)}}} \cdot \frac{\pi \cdot d^2}{4} \cdot \frac{\sqrt{\boldsymbol{2}}}{\boldsymbol{2}} (\Delta \boldsymbol{p})^{-\frac{\boldsymbol{1}}{\boldsymbol{2}}} \qquad (2.5a)$$

Uncertainty due to flow density before orifice ρ_1

$$\frac{\partial q_m}{\partial \rho_1} = \frac{C \cdot \varepsilon}{\sqrt{\Delta p \cdot (1-\beta^4)}} \cdot \frac{\pi \cdot d^2}{4} \cdot \frac{2}{2} \cdot \frac{\sqrt{2}}{2} \cdot (\rho_1)^{-\frac{1}{2}}$$

$$= \frac{\boldsymbol{C \cdot \varepsilon}}{\sqrt{\boldsymbol{\Delta p \cdot (1-\beta^4)}}} \cdot \frac{\boldsymbol{\pi \cdot d^2}}{\boldsymbol{4}} \cdot \frac{\sqrt{\boldsymbol{2}}}{\boldsymbol{2}} \cdot (\boldsymbol{\rho_1})^{-\frac{\boldsymbol{1}}{\boldsymbol{2}}} \qquad (2.5b)$$

Uncertainty due to discharge coefficient C

$$\frac{\partial q_m}{\partial C} = \frac{\boldsymbol{\varepsilon}}{\sqrt{\boldsymbol{1-\beta^4}}} \cdot \frac{\boldsymbol{\pi \cdot d^2}}{\boldsymbol{4}} \cdot \sqrt{\boldsymbol{2 \cdot \Delta p \cdot \rho_1}} \qquad (2.5c)$$

Uncertainty due to expansion factor ε

$$\frac{\partial q_m}{\partial \varepsilon} = \frac{\boldsymbol{C}}{\sqrt{\boldsymbol{1-\beta^4}}} \cdot \frac{\boldsymbol{\pi \cdot d^2}}{\boldsymbol{4}} \cdot \sqrt{\boldsymbol{2 \cdot \Delta p \cdot \rho_1}} \qquad (2.5d)$$

Plugging all the above individual uncertainties to the equation (1) and dividing it to the equation (2), we get the following result:

$$\frac{w_{q_m}}{q_m} = \left[\left(\frac{w_{\Delta p}}{2\Delta p}\right)^2 + \left(\frac{w_{\rho_1}}{2\rho_1}\right)^2 + \left(\frac{w_C}{C}\right)^2 + \left(\frac{w_\varepsilon}{\varepsilon}\right)^2\right]^{\frac{1}{2}}$$

$$= \left[\frac{1}{4}\left(\frac{w_{\Delta p}}{\Delta p}\right)^2 + \frac{1}{4}\left(\frac{w_{\rho_1}}{\rho_1}\right)^2 + \left(\frac{w_C}{C}\right)^2 + \left(\frac{w_\varepsilon}{\varepsilon}\right)^2\right]^{\frac{1}{2}}$$

For $\frac{w_{\rho_1}}{\rho_1}$:

$$p_1 = \rho_1 \cdot R \cdot T_1 \qquad (2.6)$$

$$\rho_1 = \frac{p_1}{R \cdot T_1}$$

$$\frac{d\rho_1}{dp_1} = \frac{1}{R \cdot T_1}$$

$$\frac{d\rho_1}{dT_1} = -\frac{p_1}{R \cdot {T_1}^2} = -\frac{1}{T_1} \cdot \frac{p_1}{R \cdot T_1}$$

$$\frac{w_{\rho_1}}{\rho_1} = \left[\left(\frac{w_{p_1}}{p_1}\right)^2 + \left(\frac{w_{T_1}}{T_1}\right)^2\right]^{\frac{1}{2}}$$

$$\Delta p = 17000\ Pa\ \pm 25.5\ Pa$$
$$C = 0.7 \pm 0.0035$$
$$\varepsilon = 0.9 \pm 0.0006$$
$$p_1 = 102095\ Pa \pm 143\ Pa$$
$$T_1 = 25℃ \pm 0.307℃$$

$$\frac{w_{\rho_1}}{\rho_1} = \left[\left(\frac{143\ Pa}{102095\ Pa}\right)^2 + \left(\frac{0.307℃}{25℃}\right)^2\right]^{\frac{1}{2}} = \sqrt{1.4 \cdot 10^{-3} + 1.508 \cdot 10^{-4}} = 0.03938$$

$$\frac{w_{q_m}}{q_m} = \left[\frac{1}{4} \cdot \left(\frac{25.5\ Pa}{17000\ Pa}\right)^2 + \frac{1}{4} \cdot (0.03938)^2 + \left(\frac{0.0035}{0.7}\right)^2 + \left(\frac{0.0006}{0.9}\right)^2\right]^{\frac{1}{2}}$$

$$\frac{w_{q_m}}{q_m} = \left[\frac{1}{4} \cdot (0.0015)^2 + \frac{1}{4} \cdot (0.03938)^2 + (5 \cdot 10^{-3})^2 + (6.67 \cdot 10^{-4})^2\right]^{\frac{1}{2}} \cong 0.0203$$

3. RESULTS AND DISCUSSION

3.1 Hot-wire Experiment Results

Hot-wire experiments were done with three different nozzle gemetries and in two different Reynolds numbers. Besides the geometries and Reynolds numbers differences, four different conditions were analyzed. The complete configurations can be seen in the **Table - 3.1**.

Table 3.1 Explored Configurations in hot-wire experiments

Jet Nozzle Geometries	**Reynolds number**	**Limitation Configuration (H/d_n)**	**Measurement Stations (Z/d_n)**
Circular	9600, 19200	6	0.5, 1.5, 2.5, 3.5, 4.5
30^0	9600, 19200	6	0.5, 1.5, 2.5, 3.5, 4.5
45^0	9600, 19200	6	0.5, 1.5, 2.5, 3.5, 4.5
Free Jet (Circular, 30^0, 45^0)	9600, 19200	0	0.5

Before starting to the experiments of different configurations, the first and important experiment was to check the symmetry of first four lines and the results showed that all the jets are symmetric. This result can be seen from the **Figure-3.1**. For this experiment, aimed or theoretical Reynolds number was 9600, which corresponds to the 0.05 Mach number and obtained Reynolds number from PID controller, was 9576 and corresponding Mach number was 0.052008.

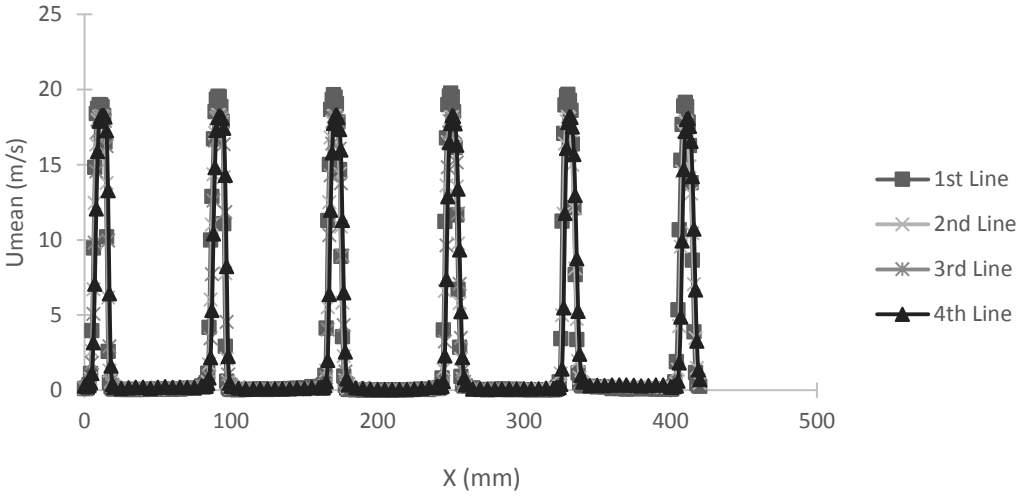

Figure 3.1 Mean Velocity Distribution for Each In-line Jet in the Jet Plate

After checking the jet-holes symmetry, passing to the different configurations. The first case is the free jet where the experiments were done without target plate to visualize the difference from the jet flow with target plate. The second case is the case where the target plate was placed to the H/d_n of 6, and by using the traverse system, the hot wire scanned both traversing between r/d_n from -15 to 15 and between Z/d_n from 0.5 to 4.5 to visualize reduction of the mean velocity distribution and also the structure of the flow. In third configuration, the hot-wire is in the $Z/d_n = 4.5$ where the hot-wire anomemeter is close to the surface, scans from the center of one jet and ends up in the center of the neighbouring jet. This aimed to analyze and visualize the interaction of two jets, how they entrain. For the fourth case, the hot-wire anomometer starts almost from the surface of the target plate where the aim is to catch the wall jet leaving either from the single or multiple jets. The last but not the least, fifth case, is the wall jet in the middle of two jets. This time, wall jet of the interaction of two jets comes into the picture. In every stage of the analyzes to conduct the controlled experiment, the flow rate, Reynolds number, Mach number, Pressure difference and Discharge Coefficient were controlled recorded and observed.

Figure-3.2 shows the first case which is the free jet, the variation of mean velocity with respect to radial direction. Graph shows the distribution for three different geometries where the maximum velocity is the highest for 30 degree nozzle but 45 degree and circular nozzles have similar maximums.

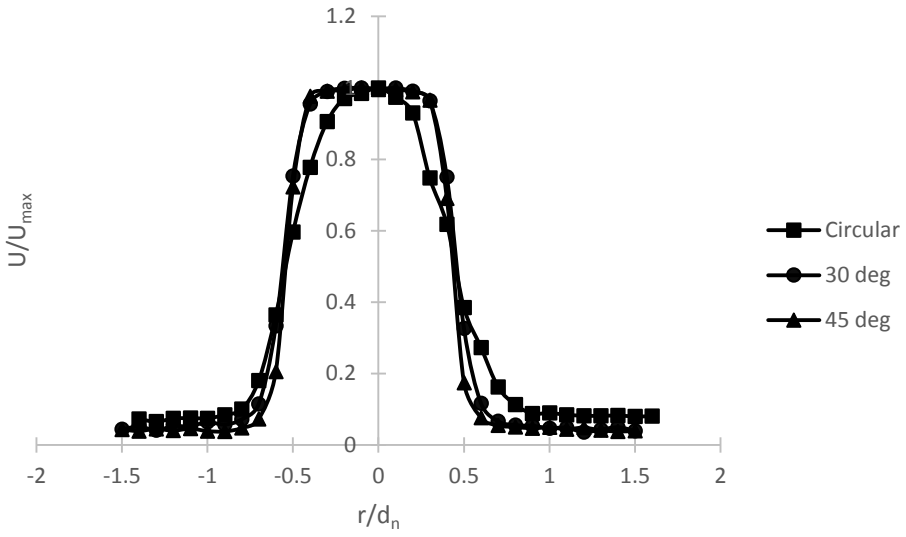

Figure 3.2 Free Jet Mean Velocity Distribution for Re = 9600, H/dn = 0

Figure-3.3 is the second case in which the target plate is placed and hot wire traverse radially between $-1.5d_n$ to $1.5d_n$ and in the Z direction it traverse from Z/d_n of 0.5 to 4.5. The graph shows the decreasing trend which is reasonable since hot-wire receding from the exit of the jet where the jet flow approaches to the target plate and slows down. First three garphs show close gaussian distribution but as the hot-wire get close to the target plate, the flow becomes more unpredictable and irregular.

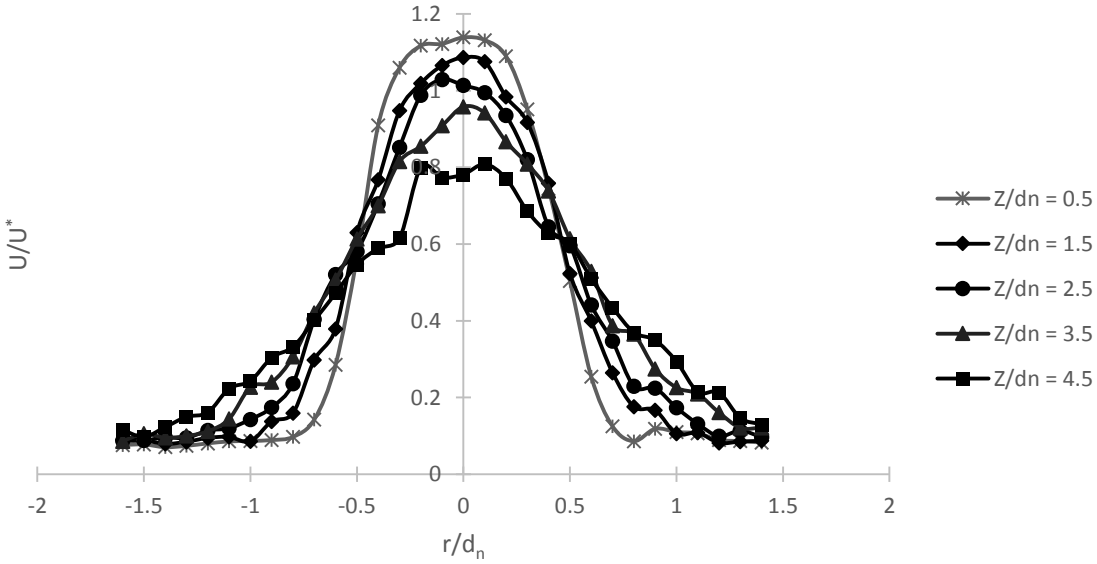

Figure 3.3 Variation of Mean Velocity Distribution for Re = 9600 , 0^0, H/dn = 6

For Re number 19200, the trend is similar to the Re number 9600 as seen from the **Figure-3.4** the mean velocity decays and the same irregularity was also observed on this flow rate. Another observable difference is that in this case the bell shape is more prominent.

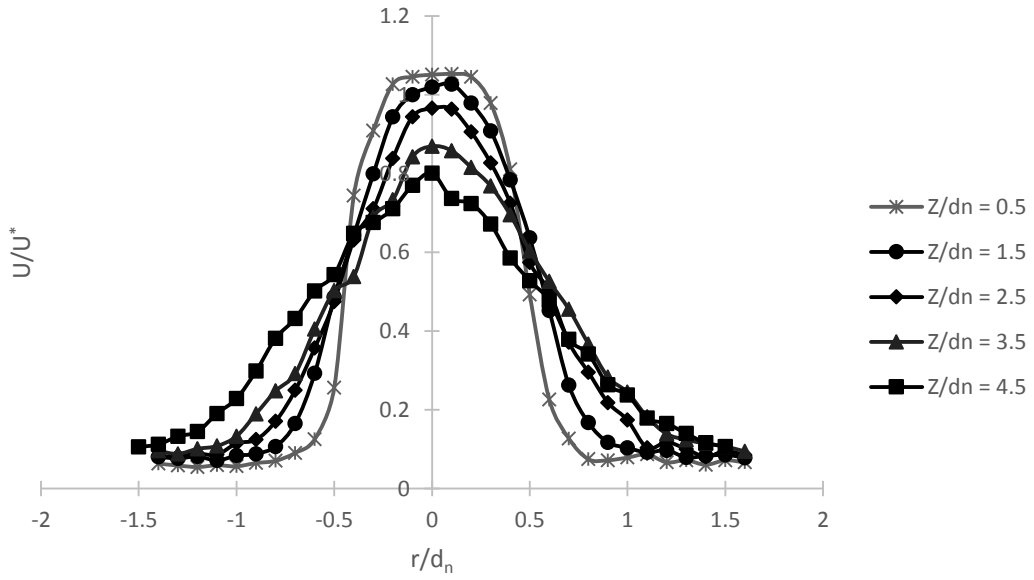

Figure 3.4 Variation of Mean Velocity Distribution for Re = 19200, 0^0, H/dn = 6

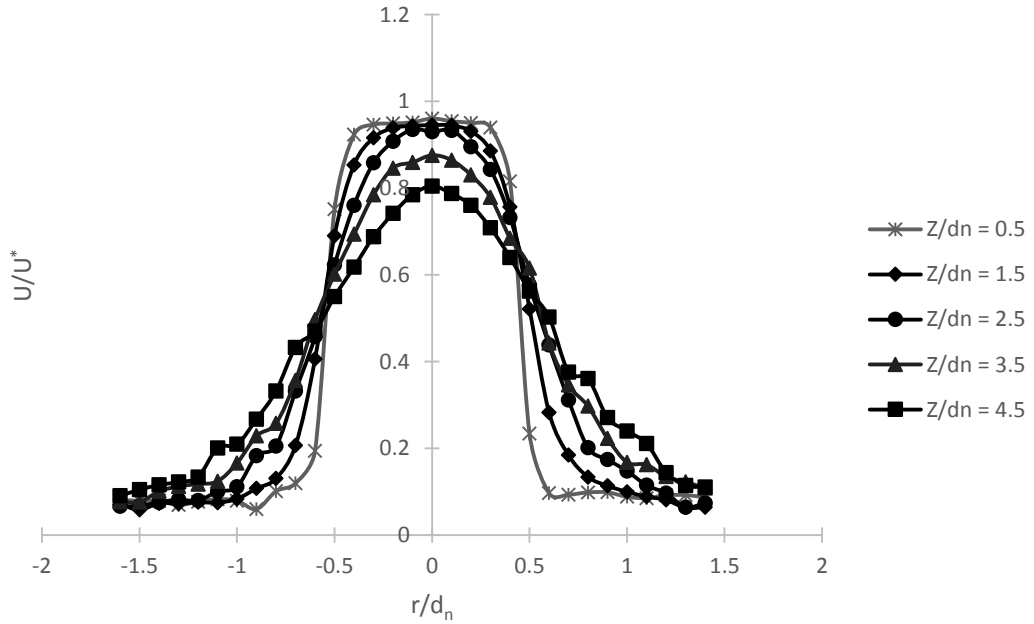

Figure 3.5 Variation of Mean Velocity Distribution for Re = 9600, 30^0, H/dn = 6

Different than the conventional circular geometry, (**Figure – 3.6**, **3.7** and **3.8**) the flat velocity distribution can be observed in 30 and 45 degree nozzles which is the result of the differential pressure type of nozzle (Zuckerman et. al.).

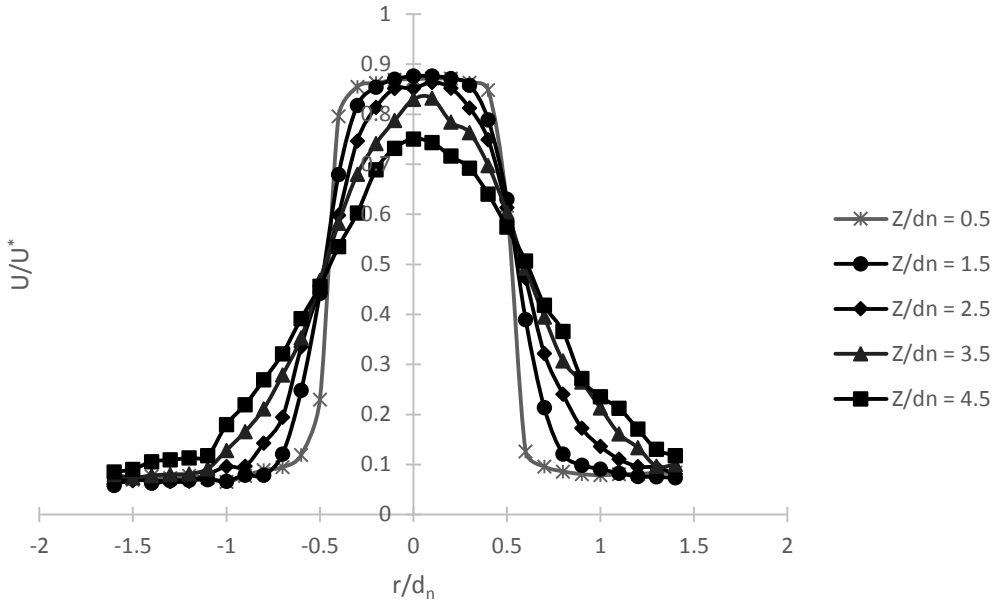

Figure 3.6 Variation of Mean Velocity Distribution for 19200, 30^0, H/dn = 6

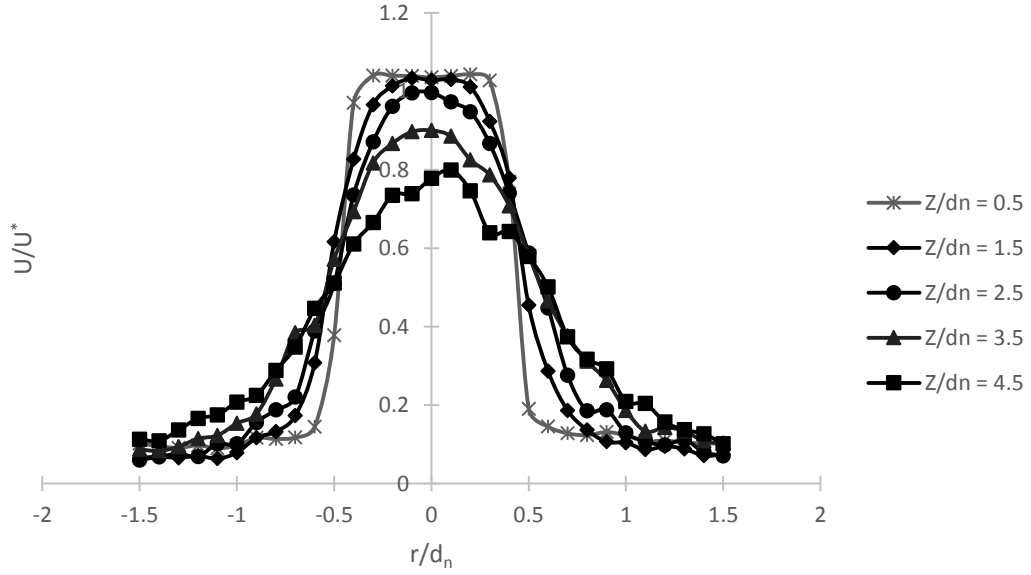

Figure 3.7 Variation of Mean Velocity Distribution for Re = 9600, 45^0, H/dn = 6

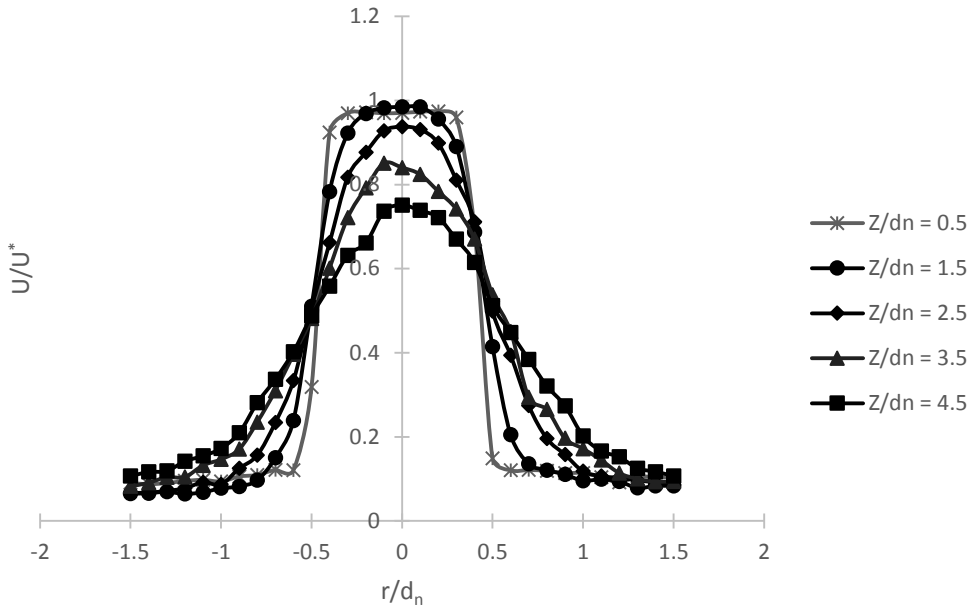

Figure 3.8 Variation of Mean Velocity Distribution for Re = 19200, 45^0, H/dn = 6

In order to analyse the graphs that were presented in **Figure 3.6** to **3.8**, centreline velocities versus vertical stations Z/d_n were plotted in **Figure –3.9** and **3.10**. It can be observed mostly that due to the contraction, flow in 30 and 45 degree nozzles, flow accelerates inside the nozzle and centreline velocity keeps increasing as it leaves the nozzle which can be observed more clearly in the case of Reynolds number of 19200. Comparing also circular nozzle with two nozzle angles, reveals that centreline velocity of the circular nozzle is greater than the 30 and 45 degree nozzles which can be the direct result of the separation due to the reduced effective area at the exit of the nozzle. Analysis on the centreline velocities also revealed that 30 degree nozzle has the longest core region. In addition to the core region, the centreline velocity decay rate is lower for the 30 degree jet nozzle which has a direct influence on entrainment. Also from the **Figure-3.11** it can be seen that the spreading velocities for the circular nozzle were found greater than the other nozzles. Therefore, the entrainment for the circular nozzle is better than the other nozzles.

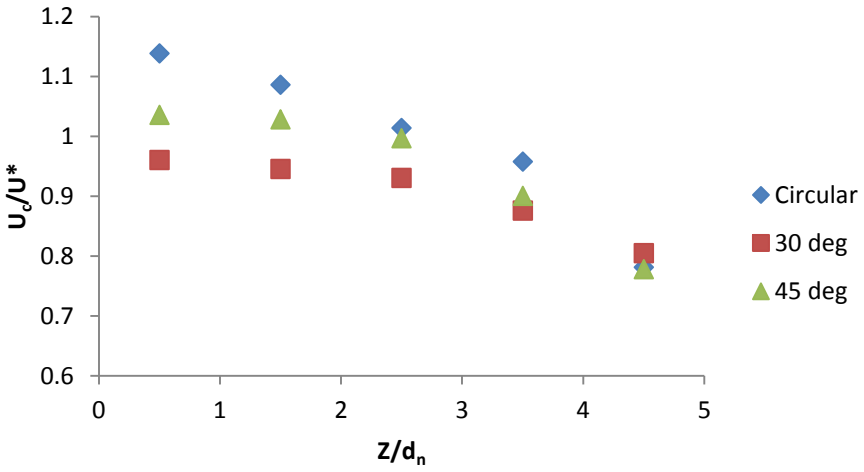

Figure 3.9 Non-dimensional centerline velocity distribution with hot-wire stations, Re = 9600, H/dn = 6

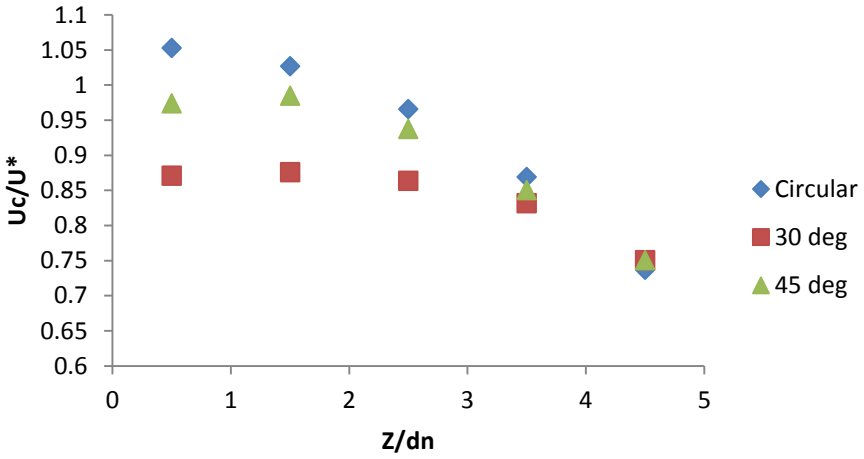

Figure 3.10 Non-dimensional centerline velocity distribution with hot-wire stations, Re = 9600, H/dn = 6

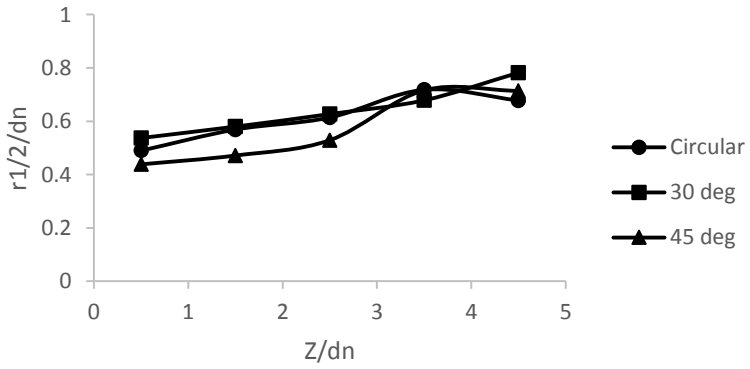

Figure 3.11 Spreading rate for different jet nozzles, Re = 19200, H/dn = 6

Figure - 3.12 shows the mean velocity distribution for the hot-wire position of Z/d_n = 0.5. It can be observed from the graph that for the given position, the circular nozzle have the highest maximum velocity, then comes the 45 and 30 degree nozzles. This region is right after the exit which corresponds to the potential core, where the exit velocity distribution is uniform.

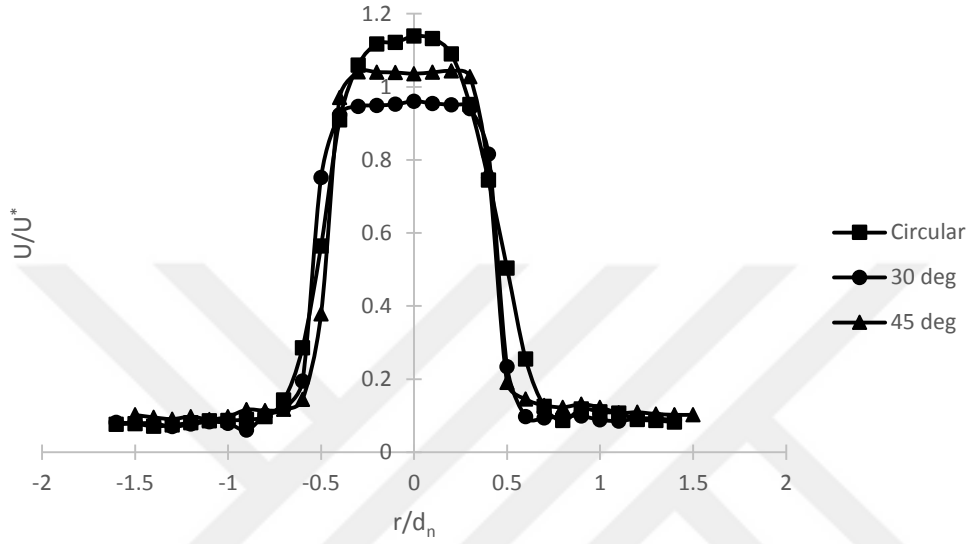

Figure 3.12 Variation of mean velocity ditribution for station Z/dn = 0.5 and Re = 9600, $H/d_n = 6$

Figure - 3.13 shows the mean velocity distribution for the hot-wire anomometer position of Z/d_n = 1.5.This station is also corresponds to the potential core region. Different than the previous case, the graph shows the same behaviour but only difference is that 45 degree nozzle distribution getting closer to the circular one .

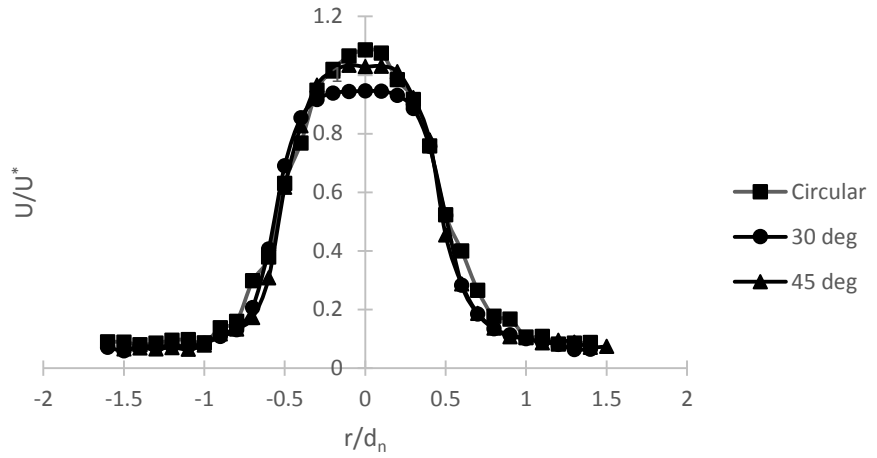

Figure 3.13 Variation of mean velocity ditribution for station Z/dn = 1.5 and Re = 9600 $H/d_n = 6$

Figure – 3.14 and **3.15**, passing to the non-dimensional vertical distances of 2.5 and 3.5, the flow still in early stages of its development where the jet flow pass from underdeveloped to developed region. However, considering the previous stations, as the hot-wire moves away from the exit, the velocity distribution of three nozzle geometries get closer.

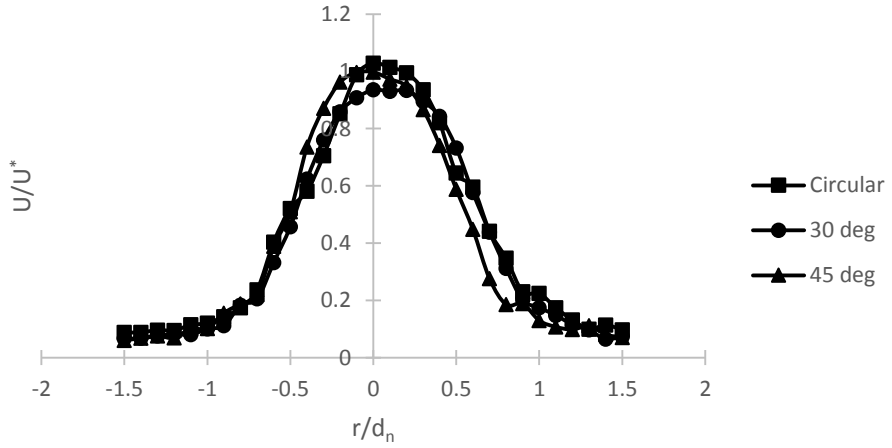

Figure 3.14 Variation of mean velocity ditribution for station Z/dn = 2.5 and Re = 9600 H/dn = 6

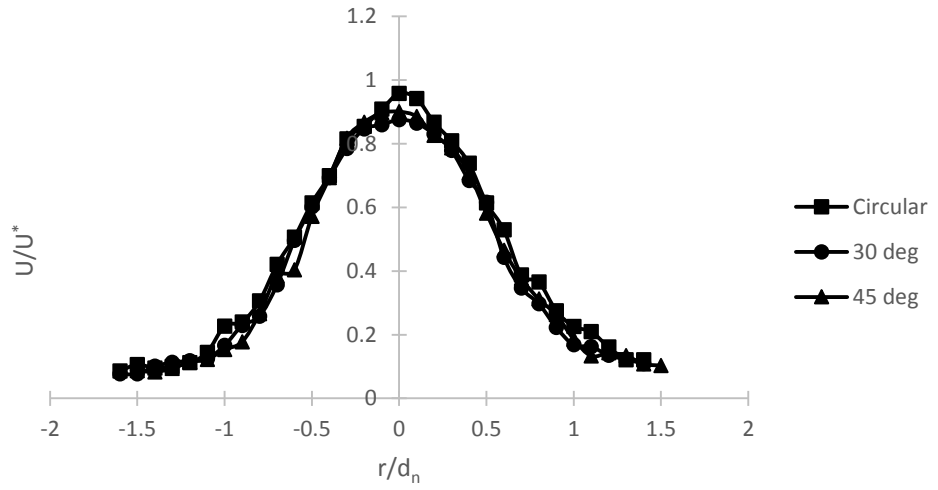

Figure 3.15 Variation of mean velocity ditribution for station Z/dn = 3.5 and Re = 9600, H/dn = 6

The **Figure - 3.16** shows the final station of the hot-wire where the potential core almost vanishes where the flow becomes developed and at the same time more turbulent because of the entrainment with ambient air. This turbulence can be seen more obviously in 45 dgeree nozzle.

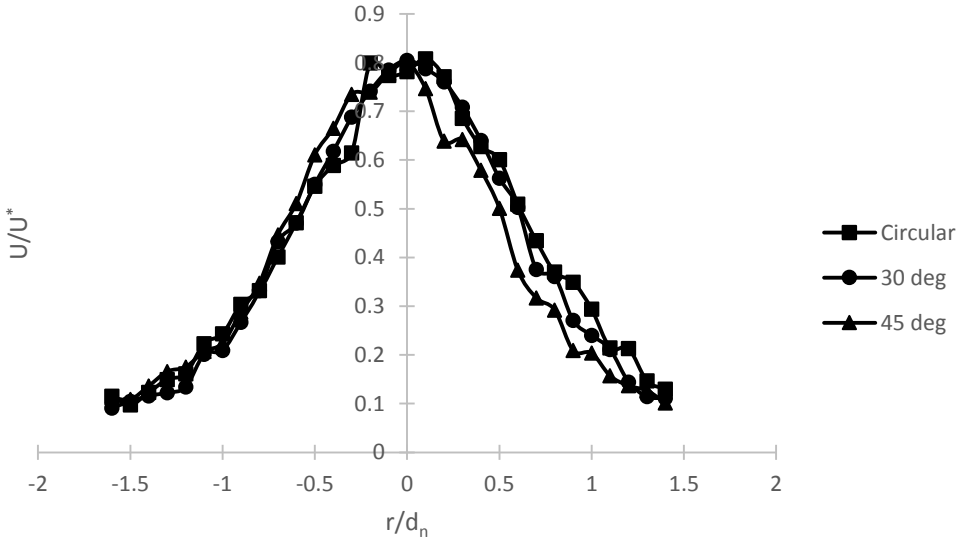

Figure 3.16 Variation of mean velocity ditribution for station Z/dn = 4.5 and Re = 9600, H/dn = 6

Figure – 3.17 and **3.18** shows the third case where the hot-wire anemometer records the veocity distribution between two jets. The aim is to show the interaction between these two jets. By interacting of two wall jets, generate the fountain upwash flow. For both Reynolds number the trend is the same but upwash flow generated by the 45 degree and circular nozzle are higher than the 30 degree nozzle. The fountain upwahs flow that are generated by the 45 degree and circular nozzles are almost smiliar. Additionally, it can also be observed that the increase of the Reynolds number causes a slight reduction in the maximum upwash flow.

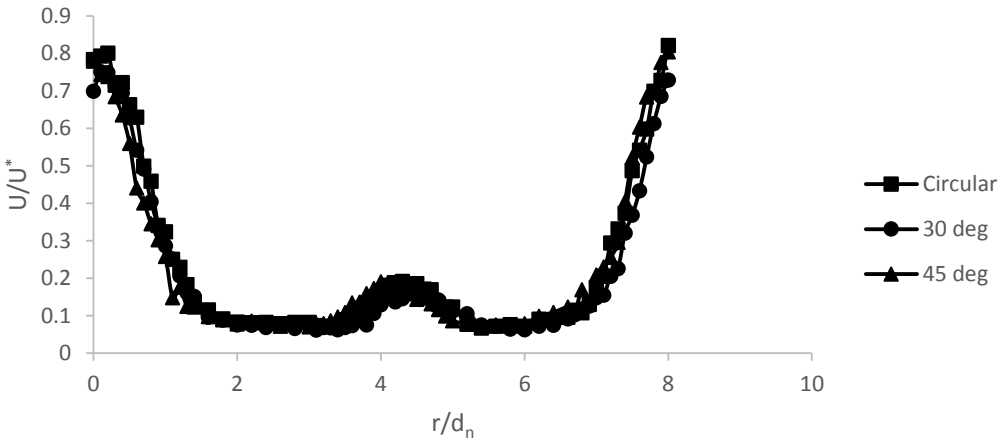

Figure 3.17 Jet Interaction for Flow Rate Re = 9600, H/dn = 6

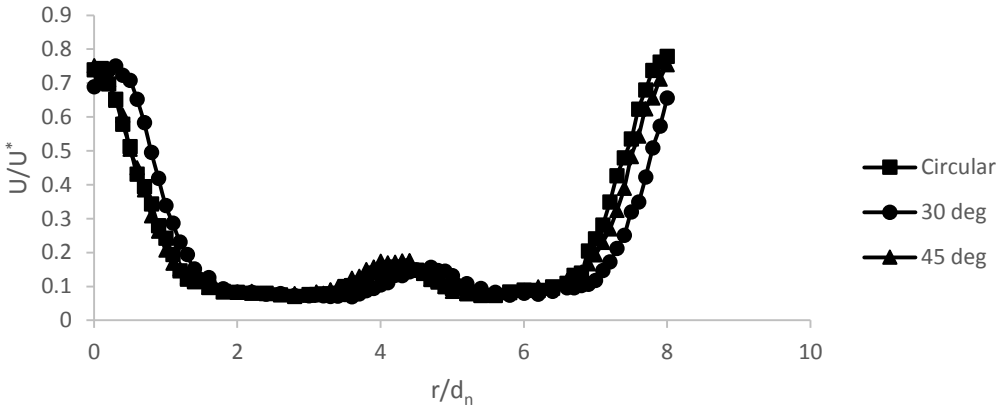

Figure 3.18 Jet Interaction for Flow Rate Re = 19200, H/dn = 6

Figure-3.19 and **3.20** represents the fourth case where the hot-wire anemometer placed both in front of the jet in crossflow and on the target plate so that the leaving boundary

layer from the cross-flow can be visualized. As seen from the graphs, for lower Reynolds number, there is slight shift for 30^0 geometry which refined for higher Reynolds number. What is more, it can be derived from the grapgs that the overall results for the measurments that are taken far from the jet exit, shows the similar results. In other words, difference in the jet nozzle geometry did not influence the remote region of the jet center, it only has an effect on the zone of interior.

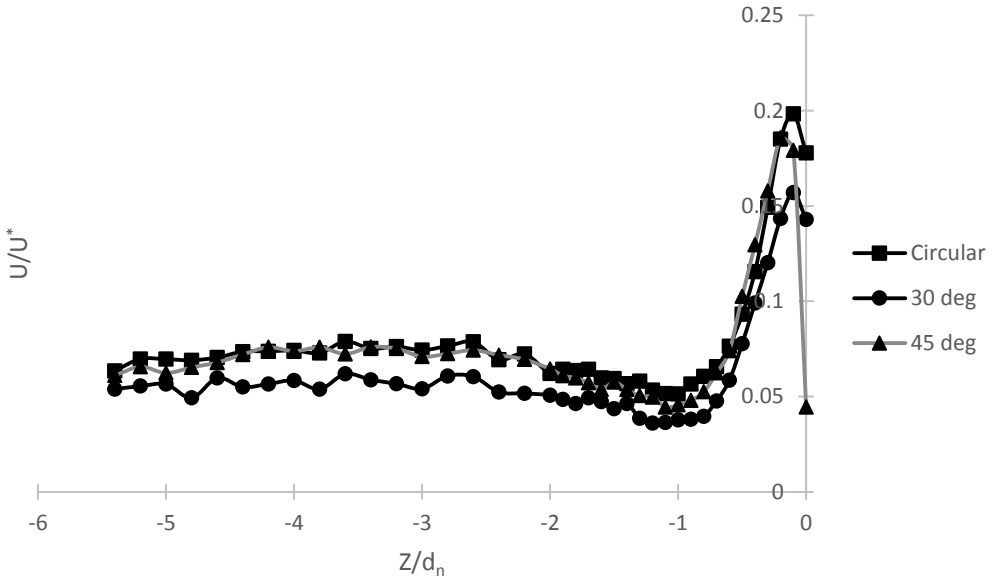

Figure 3.19 Wall Jet In front of the Jet at Re = 9600, H/dn = 6

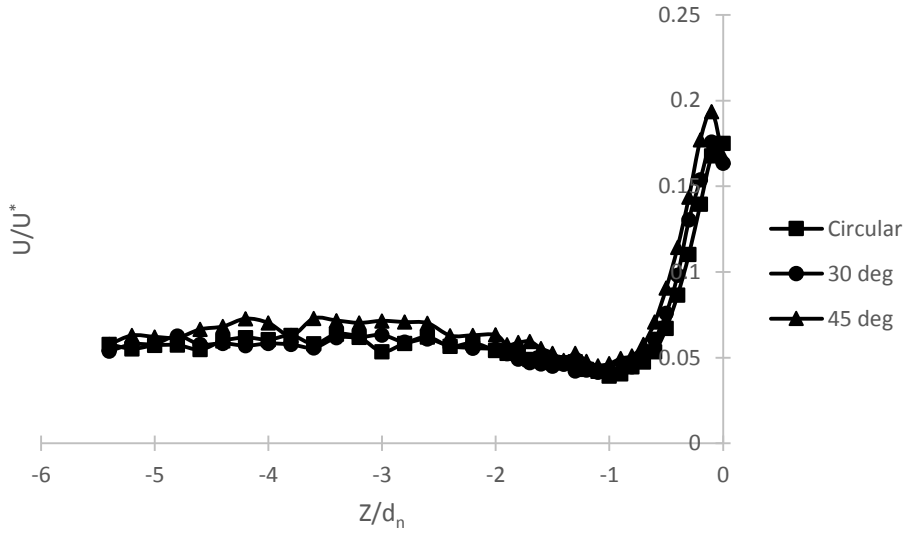

Figure 3.20 Wall Jet In front of the Jet Re = 19200, H/dn = 6

The effect of the increase of Reynolds number on wall jet was also observed in **Figuers-3.21, 3.22** and **3.23**. The only observable difference can be seen in circular nozzle where the increase of Reynolds number positively affects the thickness of the wall jet. In other geometries, the increase of the Reynolds number did not affect the wall jet thickness.

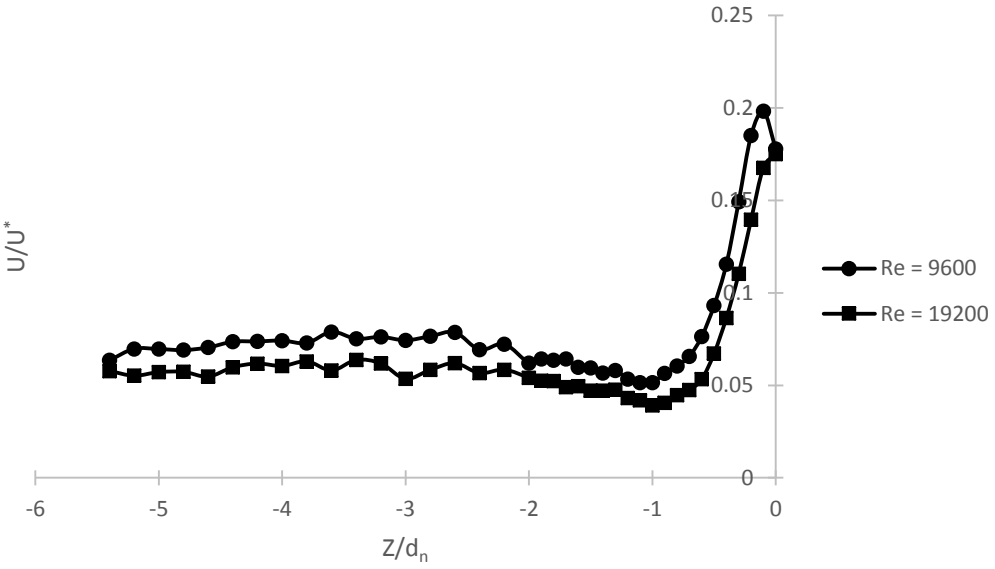

Figure 3.21 Wall Jet In front of the Jet, Circular nozzle and H/dn = 6

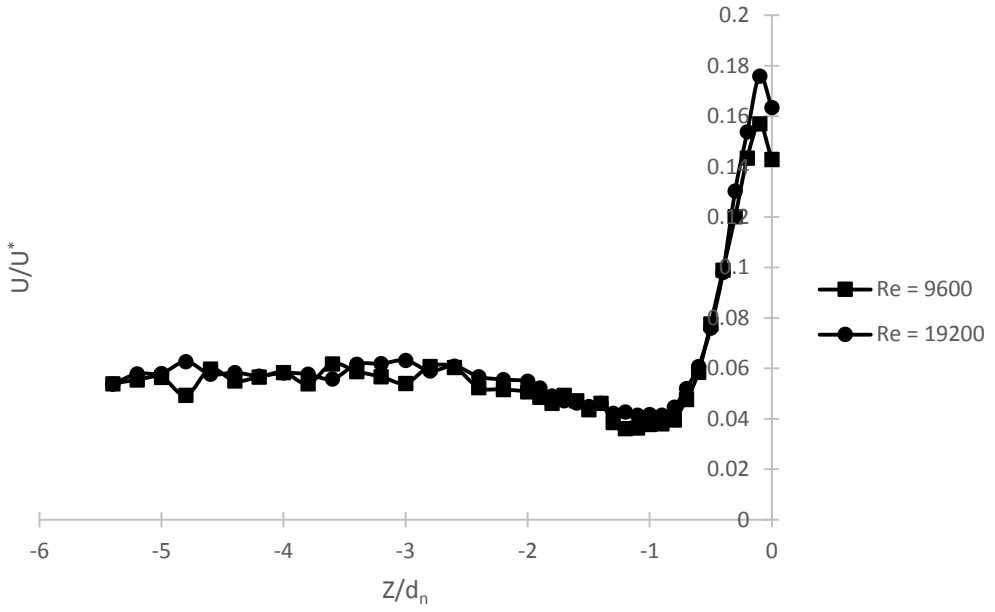

Figure 3.22 Wall Jet In front of the Jet, 300 nozzle and H/dn = 6

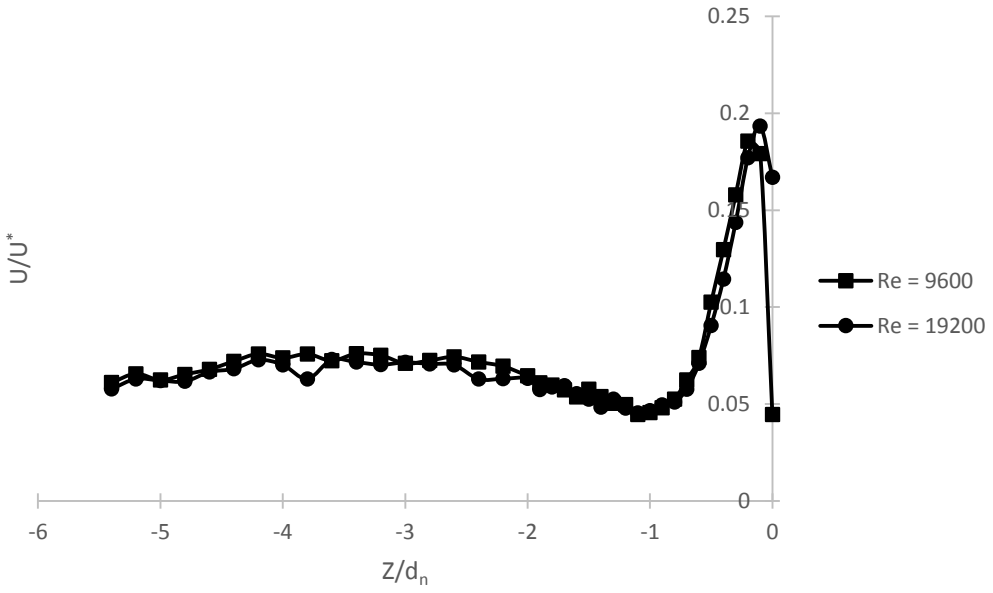

Figure 3.23 Wall Jet In front of the Jet, 450 nozzle and $H/d_n = 6$

3.2 Pressure Measurment Results

The pressure measurments were done in three different geometries, two Reynolds number and three different jet-to-target spacing. Data acquasation was done by the 32 channel pressure scanner. **Table – 3.2** shows the varying parameters in the experiment

Table 3.2 Pressure scanning configurations

Jet Geometries	**Reynolds Numbers**	**Limitation Configuration (H/d_n)**
0^0	9600, 19200	4, 6, 10
30^0		
45^0		

Figure – 3.24 shows the jet plate and the jet location which measurments visualized and graphed. The surrounding region of the jet was coded with letters and the streamwise location corresponds to the letter E and the spanwise location corresponds to the letter B.

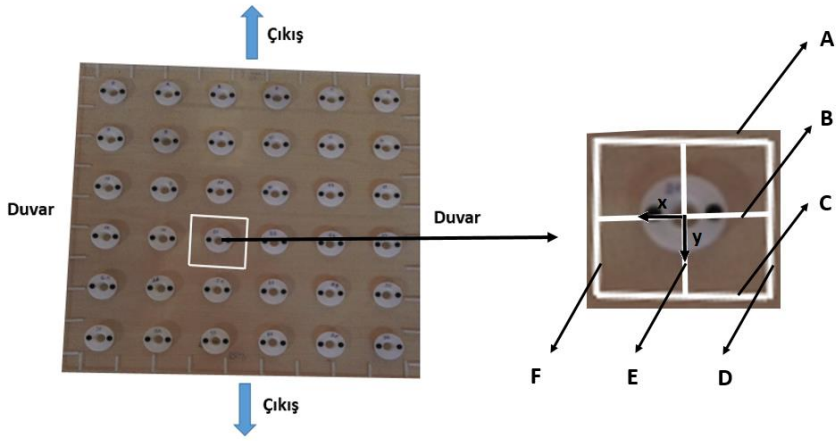

Figure 3.24 Measurment lines of the pressure scanner in the jet plate

Figure – 3.25, 3.26, 3.27, 3.28, B1 and **B2 (Appendix B)** represents the pressure distribution for the case where the H/dn is 4 and the Reynolds number is 19200. Both streamwise and spanwise pressure distribution and also the region that the jet spreaded. Analyzing the graphs showed that for both direction, spanwise and streamwise, the pressure distributions are similar for all geometries. However, it was observed that there is a direct relationship between chamfering angle and maximum pressure which can be seen from the graphs that as the angle increases, the maximum pressure also increases. In addition, despite of the similarities of the spanwise and streamwise distribution, the graphs showed that different than spanwise, in streamwise direction, the three geometries converge to each other faster than the spanwise. As a result, it was deduced from the results that chamfering angle only affected the maxium pressure values and has no any influence on jet impingement area.

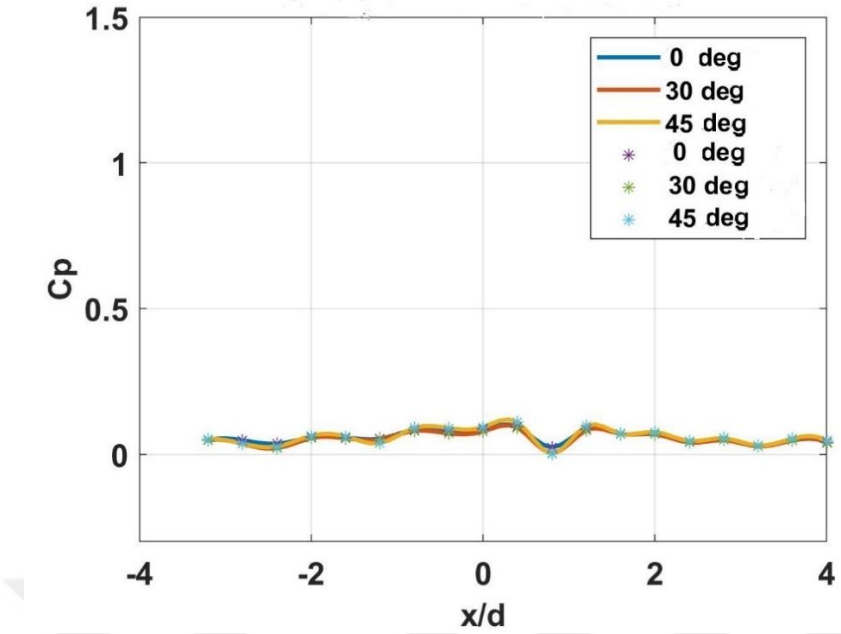

Figure 3.25 $H/d_n = 4$ Re=19200 – Pressure distribution along the line A

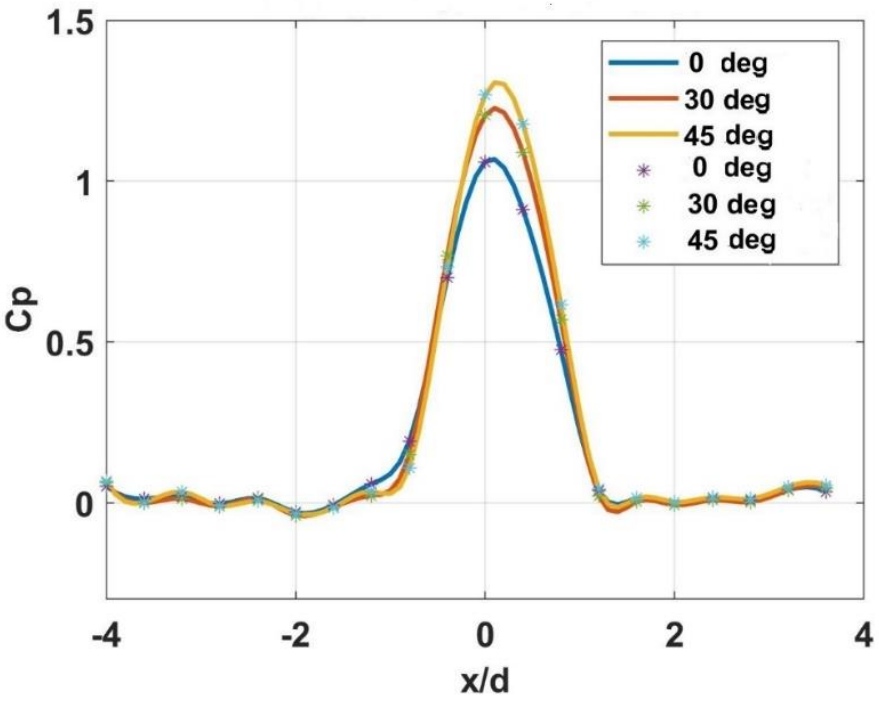

Figure 3.26 $H/d_n = 4$ Re=19200 – Pressure distribution along the line B

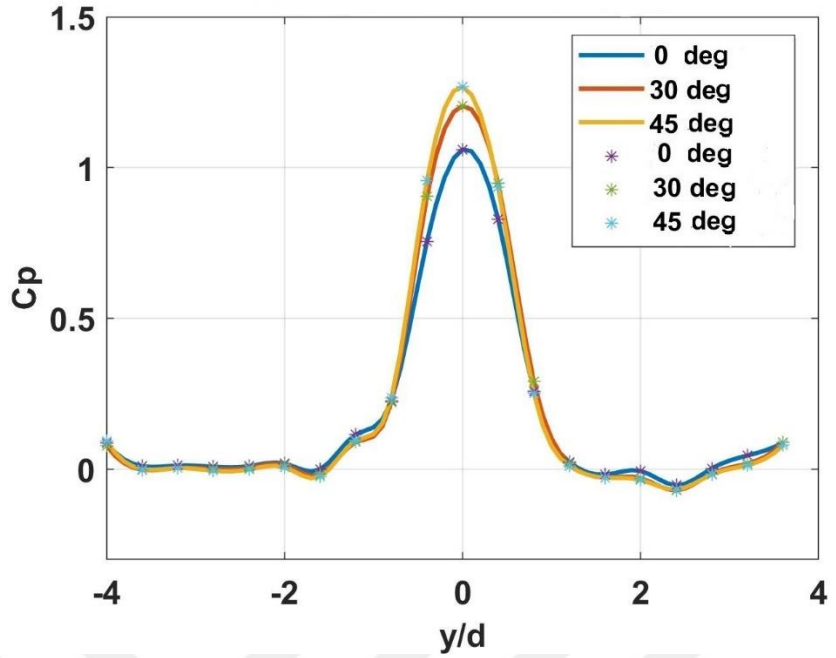

Figure 3.27 H/d_n = 4 Re = 19200 – Pressure distribution along the line E

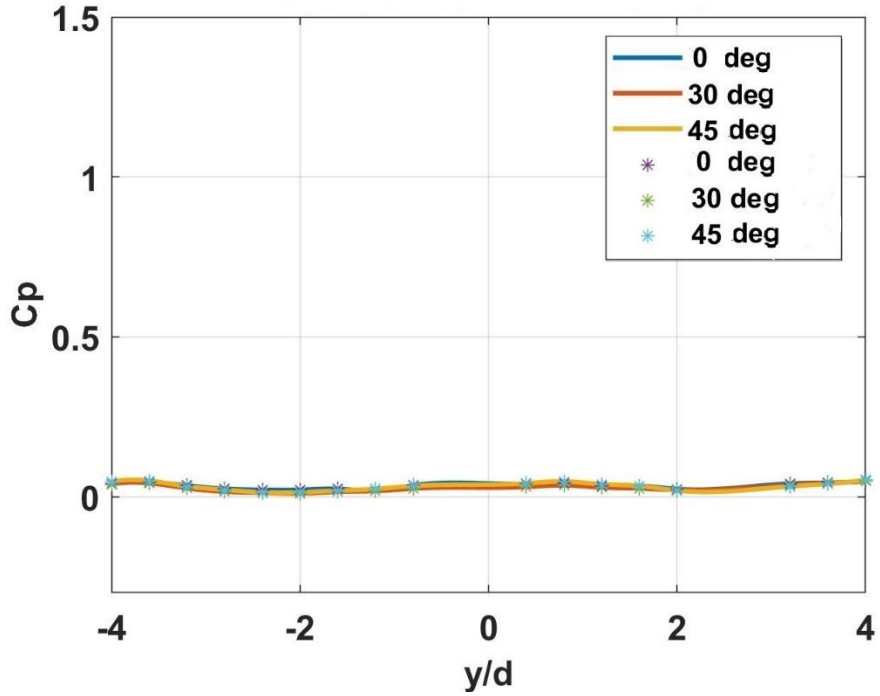

Figure 3.28 H/d_n = 4 Re = 19200 – Pressure distribution along the line F

The pressure distribution for H/dn = 6 and Re = 19200 were shown in the **Figure** – **3.29, 3.30, 3.31, 3.32, B3** and **B4 (Appendix B)**. Similarly, the stagnation and jet impingement area were shown with the letters A, B, C, D, E and F.

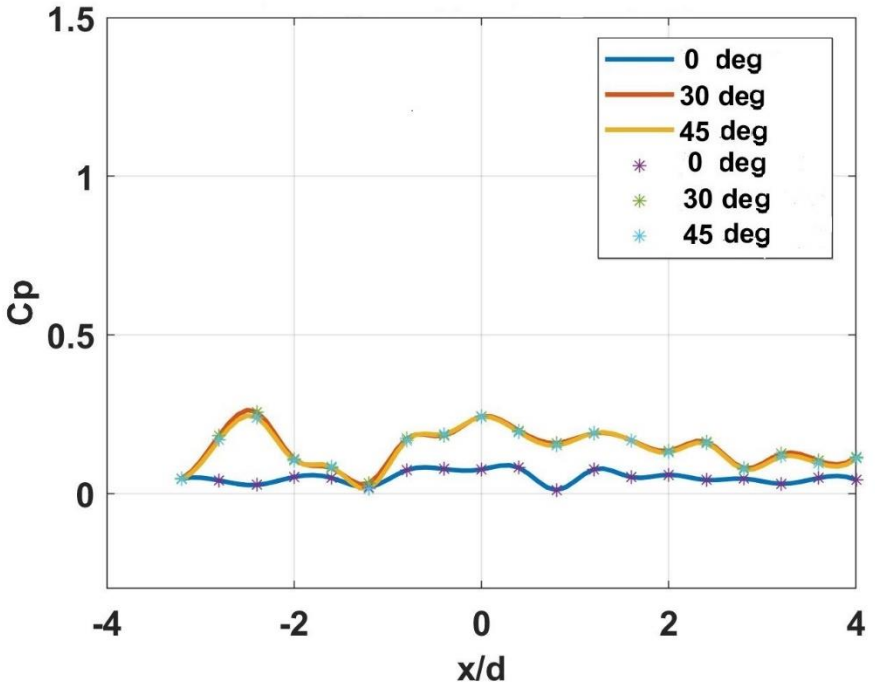

Figure 3.29 $H/d_n = 6$ Re = 19200 – Pressure distribution along the line A

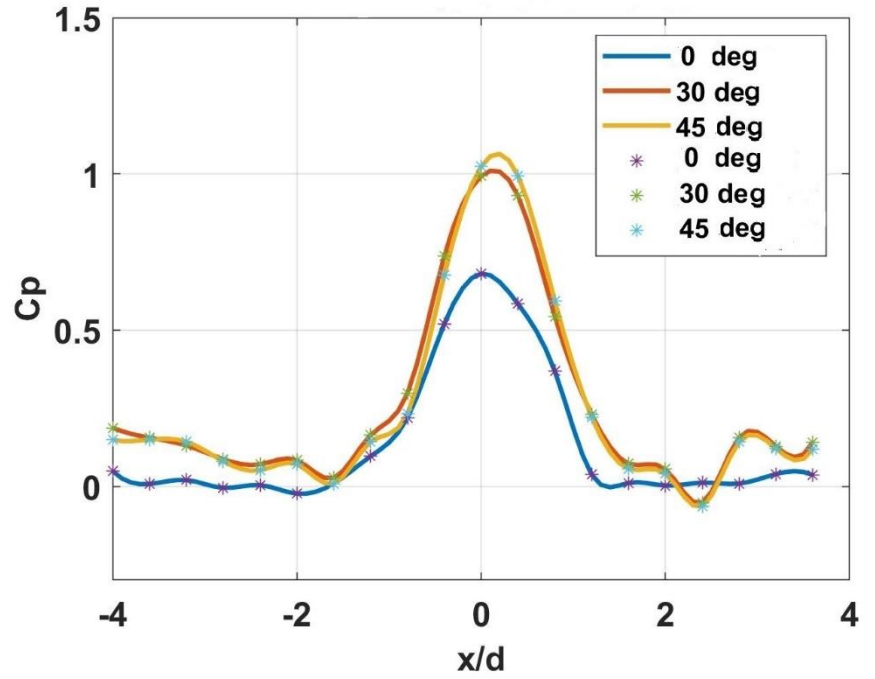

Figure 3.30 $H/d_n = 6$ Re = 19200 – Pressure distribution along the line B

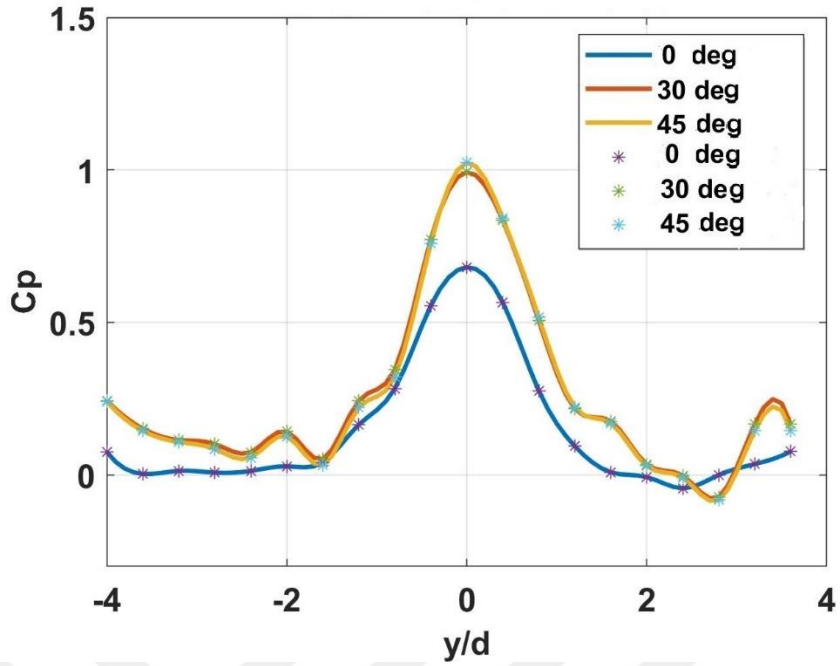

Figure 3.31 H/d_n= 6 Re = 19200 – Pressure distribution along the line E

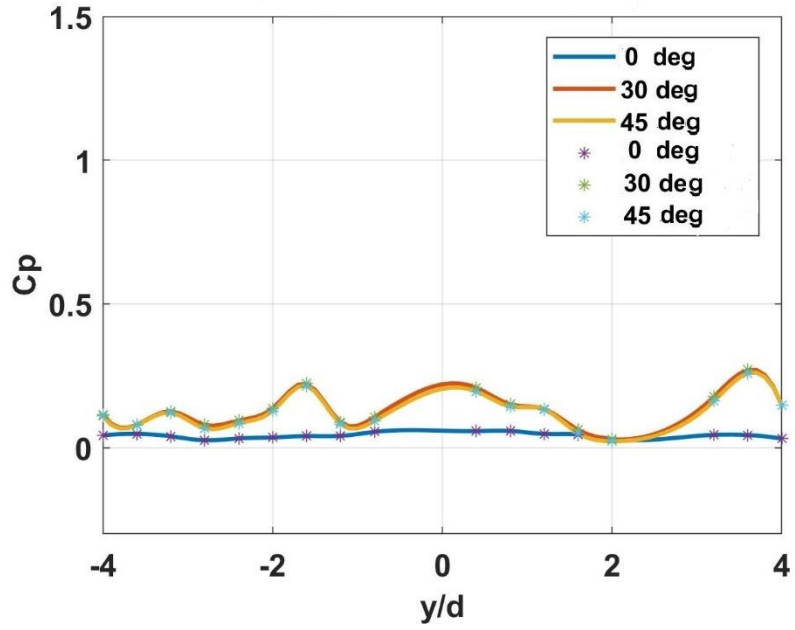

Figure 3.32 H/d_n = 6 Re = 19200 – Pressure distribution along the line F

It can be observed from the graphs that along the line A, C, D and F, 30^0 and 45^0 jets show similar trend but in the circular one the pressure values are lower than the other two geometries. Additionally, the pressure distribution along the line B for 30^0 and 45^0 geometries showed the same trend and the maximum impinging pressures are shifted from the geometric center of the channel. On the other hand, for the circular geometry

the pressure measurments are lower than the other geometries and the maximum pressure coincides with the geometric center ($x/d_n = 0$) in the spanwise direction. In addition, the investigating of the graphs show that the impingement area for the circular geometry is shorter than the impingement area in the wall region of the 30 degree and 45 degree geometries. As the measurment line E analyzed, it is oserved that the maximum pressure value of the impinging jet is in the geometric center of the scanner. While for the upstream direction the impingement area starts at the same point for all jet geometries, in the downstream region 30^0 and 45^0 jet geometries starts at the similar point but ends at much more further away.

4. CONCLUSIONS AND RECOMMENDATIONS

This investigation observed how the chamfering angle affects the velocity and pressure distribution. The experimental work started by building the experimental set-up and then writing the proper LabVIEW program for controlling the flowrate which helped to conduct the controlled experiment. Jet nozzle geometry design was the following task which was decided by conducting the thorough literature review on jet impingement cooling. First hot-wire experiments were done in two different Reynolds number and in five hot-wire position. The results show that different than the circular geometry, 30^0 and 45^0 geometries exhibit a fairly flat velocity profile. This jet behaviour was mentioned in the work done by Zuckerman et. al. where it was stated that in the case of pipe shaped or cylindrical nozzle, the velocity profile is mostly parabolic and moderate amount of turbulence developed in the upstream; however, for the differential pressure type nozzles, the flow demonstrate a flat velocity profile with less turbulence, turns back to the parabolic far from the exit. Same results was obtained by Lee et. al. and demonstarted that orifice nozzles produce higher heat transfer rates than a fully developed pipe type nozzles where local Nu number increases of up to 65% at $H/d_n = 2$ and up to 30% at $H/d_n = 10$. Additionally, comparing the maximum velocities for three nozzles and for the non-dimensional jet-to-target spacing of 6 revealed that the 30^0 jet geometry generates better performance.

Pressure distribution results for three different geometries in the spanwise and streamwise direction shows similar results but as the chamfering angle increases, the maximum pressure increases which also can be the result of orifice type nozzle geometry that gives rise to the flow acceleration and pressure difference. However, the results mostly support that due to the jet geometry difference, the surface area affected by the jet impingement is considerably low.

Since the experimental work was conducted for three different geometries, other chamfering angles also should be analyzed and optimization inbetween the angles can be performed for discovering the optimum chamfering angle. These works can also be backed up with computational analyzes. Further inestigations may be attempted to

conduct the heat transfer experiments finally validate these results and contribute to the cooling and drying technologies.

5. REFERENCES

Polat, S. (1993). Heat and mass transfer in impingement drying. Drying Technology, 11(6), 1147-1176.

Han, J. C. (2013). Fundamental gas turbine heat transfer. Journal of thermal science and engineering applications, 5(2), 021007.

Angioletti, M., Di Tommaso, R. M., Nino, E., & Ruocco, G. (2003). Simultaneous visualization of flow field and evaluation of local heat transfer by transitional impinging jets. International Journal of Heat and Mass Transfer, 46(10), 1703-1713.

Han, J. C., Dutta, S., & Ekkad, S. (2013). Gas Turbine Heat Transfer and Cooling Technology: Taylor & Francis.

Uysal, Ü., Korkmaz, Y., Sözbir, N., & Hirca, A. H. (2014). Gaz türbini kanatlari kanallarinda soğutma performansinin araştirilmasi. Journal of Aeronautics and Space Technologies (Havacilik ve Uzay Teknolojileri Dergisi), 2(7), 1-8.

Jordan, C. N., Elston, C. A., Wright, L. M., & Crites, D. C. (2013, June). Leading edge impingement with racetrack shaped jets and varying inlet supply conditions. In ASME Turbo Expo 2013: Turbine Technical Conference and Exposition (pp. V03AT12A020-V03AT12A020). American Society of Mechanical Engineers.

Sunden, B., & Xie, G. (2010). Gas turbine blade tip heat transfer and cooling: a literature survey. Heat Transfer Engineering, 31(7), 527-554.

Chyu, M. K., & Siw, S. C. (2013). Recent advances of internal cooling techniques for gas turbine airfoils. Journal of Thermal Science and Engineering Applications, 5(2), 021008.

Ostanek, J. K. (2014). Improving pin-fin heat transfer predictions using artificial neural networks. Journal of Turbomachinery, 136(5), 051010.

Shanley, A. I. (2011). Cooling systems: energy, engineering and applications. Nova Science Publishers.

Bailey, J. C., Intile, J., Fric, T. F., Tolpadi, A. K., Nirmalan, N. V., & Bunker, R. S. (2002, January). Experimental and numerical study of heat transfer in a gas turbine combustor liner. In ASME Turbo Expo 2002: Power for Land, Sea, and Air (pp. 187-197). American Society of Mechanical Engineers.

Cimbala, Yunus A.Çengel, John M. (2014). Fluid mechanics : fundamentals and applications (3rd ed.). Boston: McGraw-Hill Higher Education ISBN 978-0-07-338032-2

Perry, Robert H., W., Green, Don (2008-01-01). Perry's chemical engineers' handbook. McGraw-Hill. ISBN 0071593136.

ISO, E. (2003). Measurement of Fluid Flow by Means of Pressure Differential Devices Inserted in Circular Cross Section Conduits Running Full—Part 2: Orifice Plates. EN ISO, 5167-2.

Jennerjohn, M., Lee, J., Ren, Z., Ligrani, P., McQuilling, M., Fox, M. D., & Moon, H. K. (2016). Jet array impingement cooling local Nusselt number variations: Effects of hole array spacing, jet-to-target plate distance, and Reynolds number. Heat Transfer Research, 47(2).

Li, W., Xu, M., Ren, J., & Jiang, H. (2017). Experimental Investigation of Local and Average Heat Transfer Coefficients Under an Inline Impinging Jet Array, Including Jets With Low Impingement Distance and Inclined Angle. Journal of Heat Transfer, 139(1), 012201.

Li, W., Li, X., Yang, L., Ren, J., Jiang, H., & Ligrani, P. (2017). Effect of Reynolds Number, Hole Patterns, and Hole Inclination on Cooling Performance of an Impinging Jet Array—Part I: Convective Heat Transfer Results and Optimization. Journal of Turbomachinery, 139(4), 041002.

Popiel, C. O., & Trass, O. (1991). Visualization of a free and impinging round jet. Experimental Thermal and Fluid Science, 4(3), 253-264.

Park, J., Goodro, M., Ligrani, P., Fox, M., & Moon, H. K. (2007). Separate effects of Mach number and Reynolds number on jet array impingement heat transfer. Journal of Turbomachinery, 129(2), 269-280.

Goodro, M., Ligrani, P., Fox, M., & Moon, H. K. (2010). Mach Number, Reynolds Number, Jet Spacing Variations: Full Array of Impinging Jets. Journal of Thermophysics and Heat Transfer, 24(1), 133-144.

Metzger, D. E., Florschuetz, L. W., Takeuchi, D. I., Behee, R. D., & Berry, R. A. (1979). Heat transfer characteristics for inline and staggered arrays of circular jets with crossflow of spent air. Journal of Heat Transfer, 101(3), 526-531.

Zuckerman, N., & Lior, N. (2006). Jet impingement heat transfer: physics, correlations, and numerical modeling. Advances in heat transfer, 39, 565-631.

6. APPENDICES

APPENDIX A: Transition flange, piping flange, pipe support, jet nozzle geometries, jet hole pad and pressure scanner

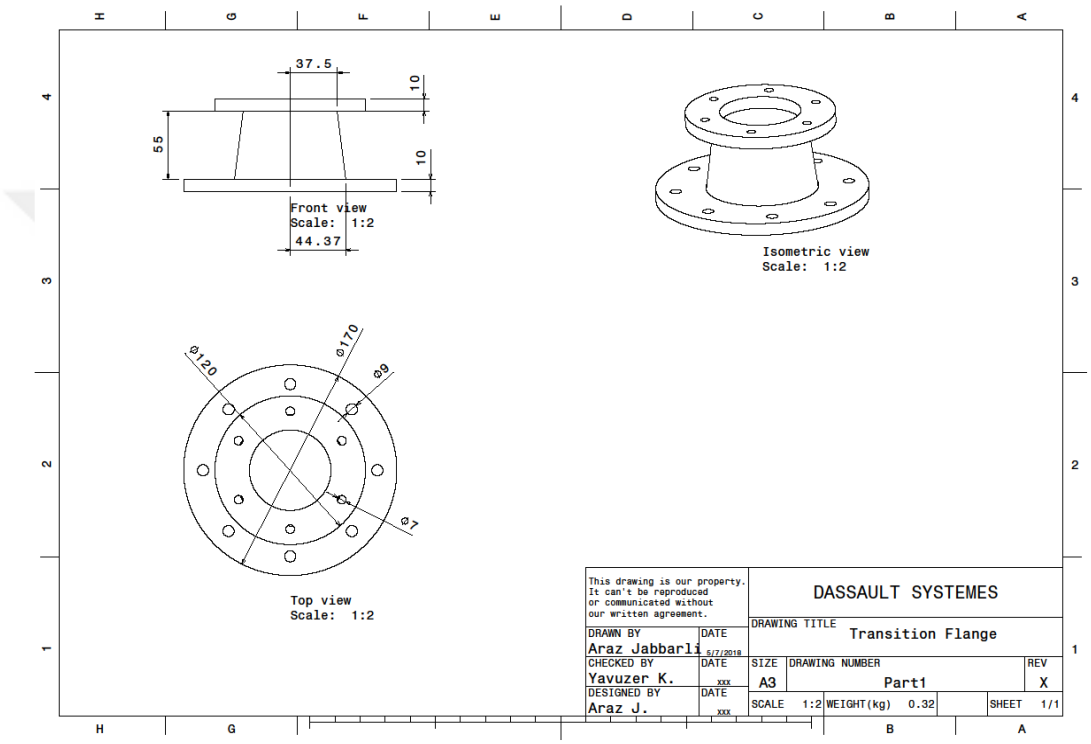

Figure A.1 Draft of transition flange

Figure A.2 Manufactured transition flange

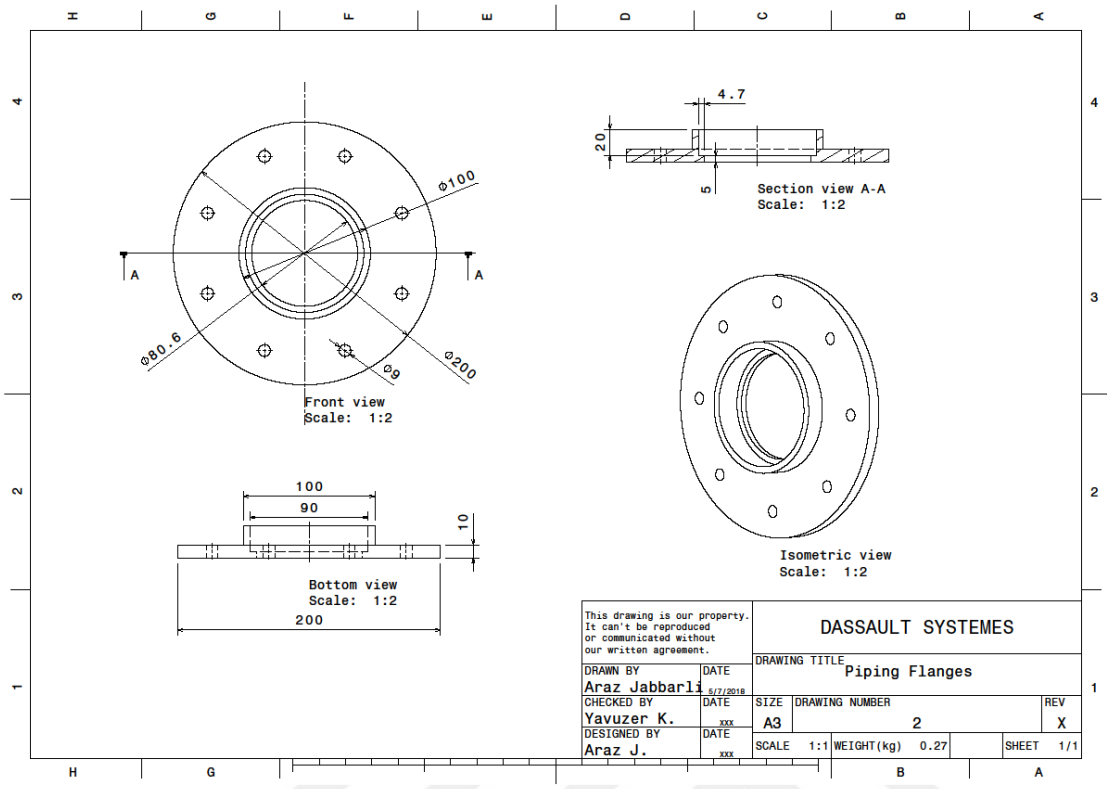

Figure A.3 Draft of piping flange

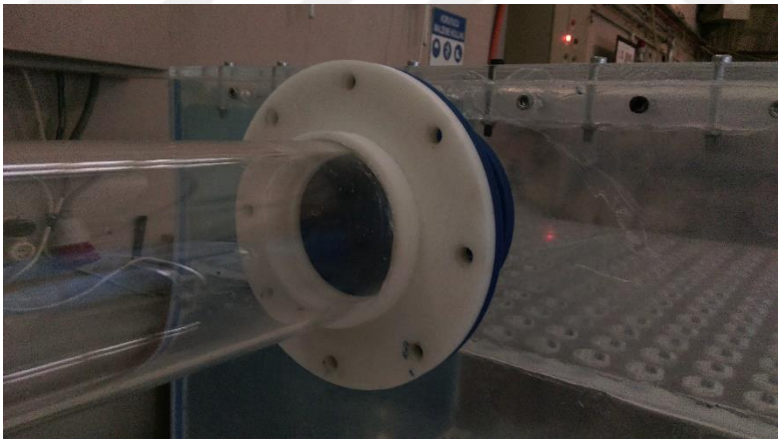

Figure A.4 Manufactured piping flange

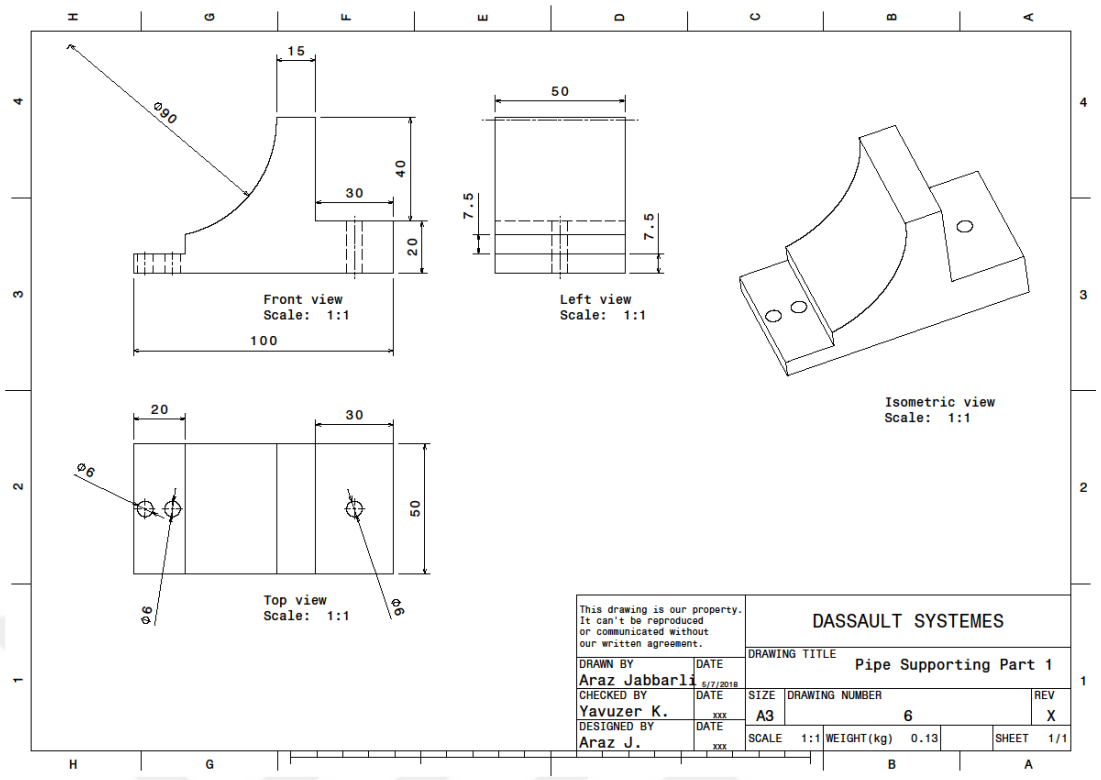

Figure A.5 Draft of pipe supporting part 1

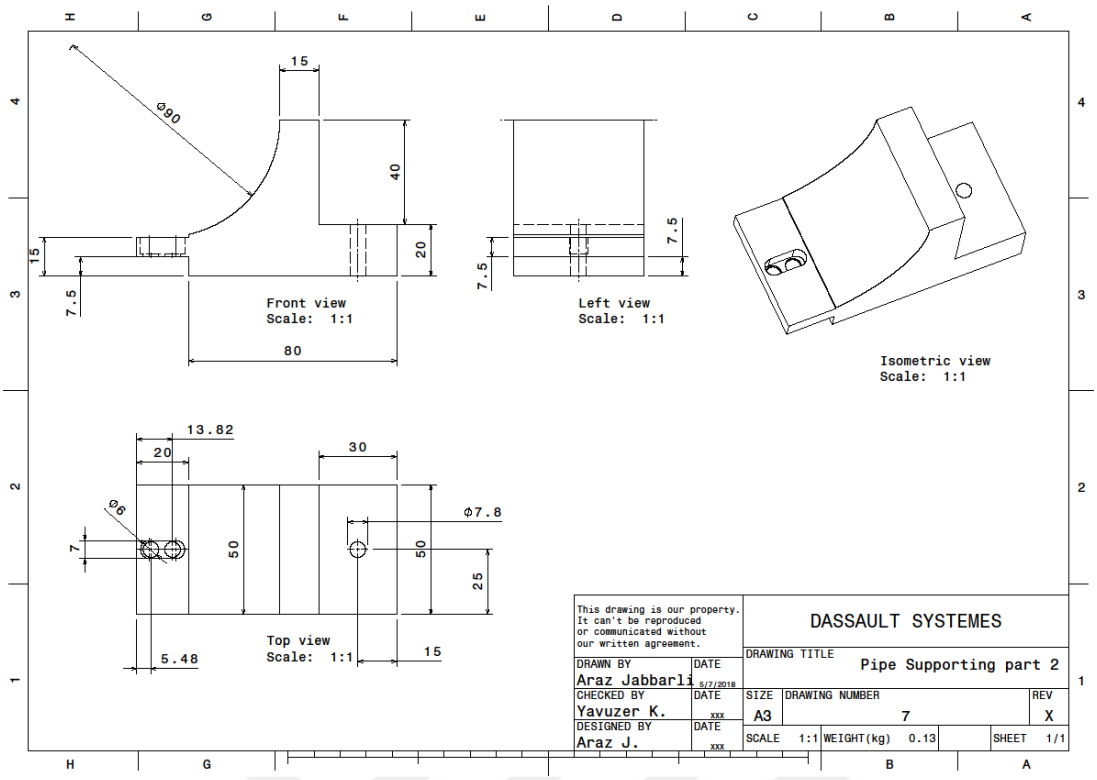

Figure A.6 Draft of pipe supporting part 2

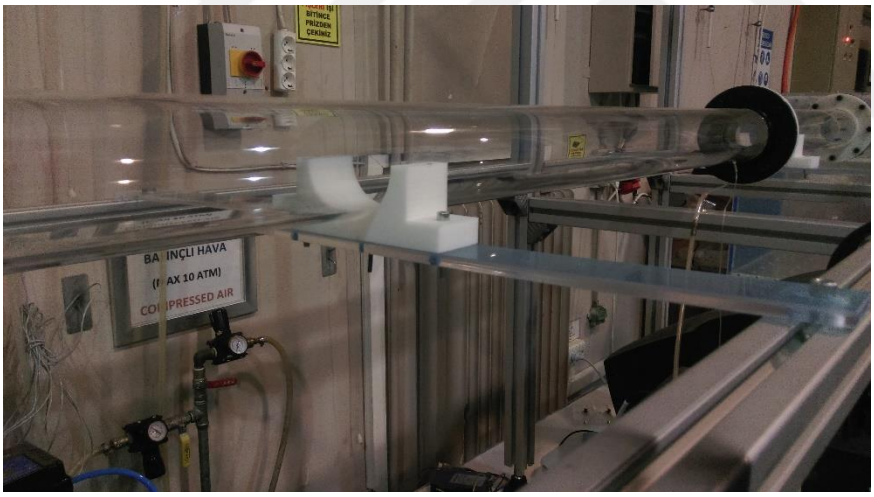

Figure A.7 Manufactured pipe supporing parts

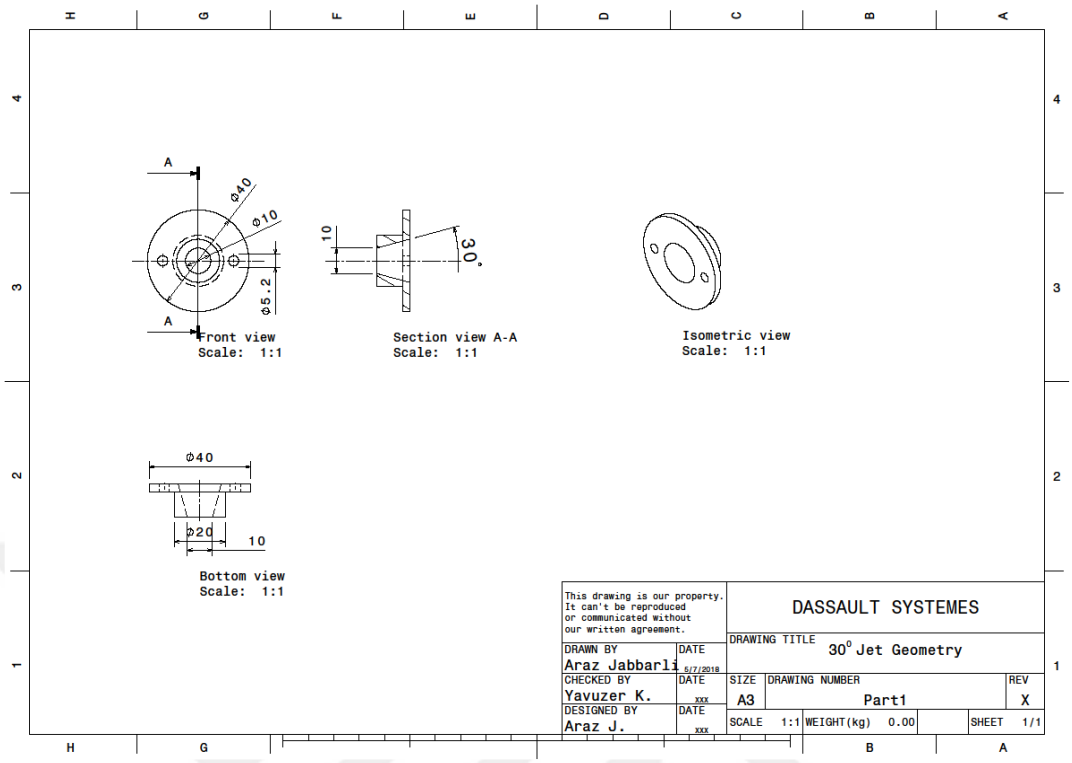

Figure A. 8 Draft of 30^0 jet nozzle

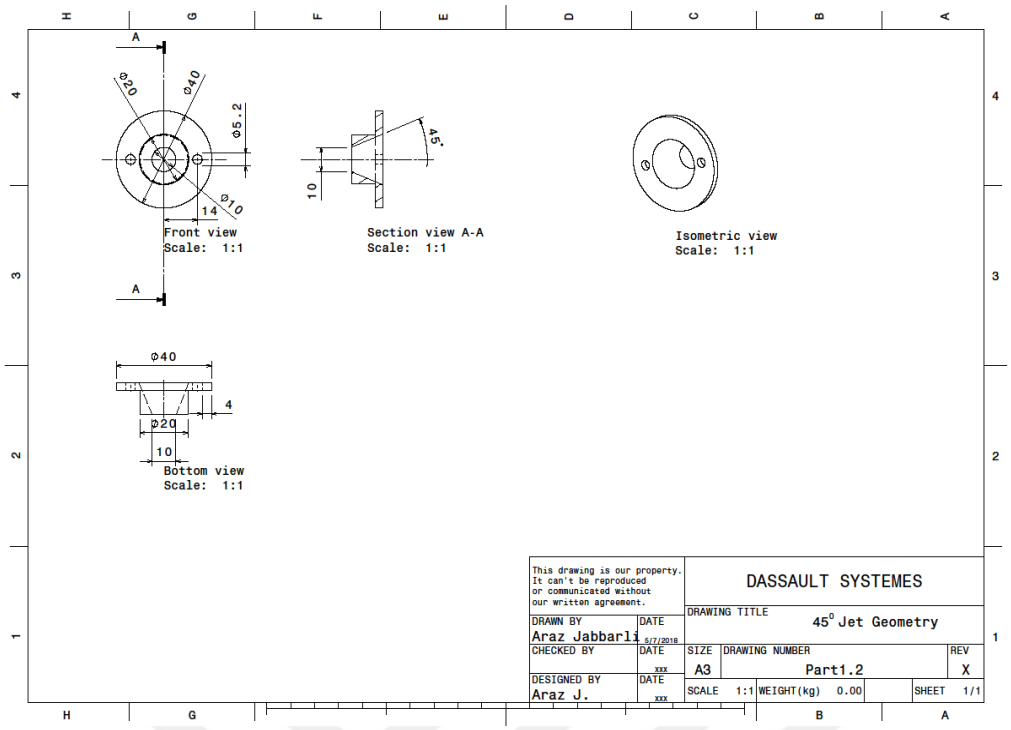

Figure A.9 Draft of 45^0 jet nozzle

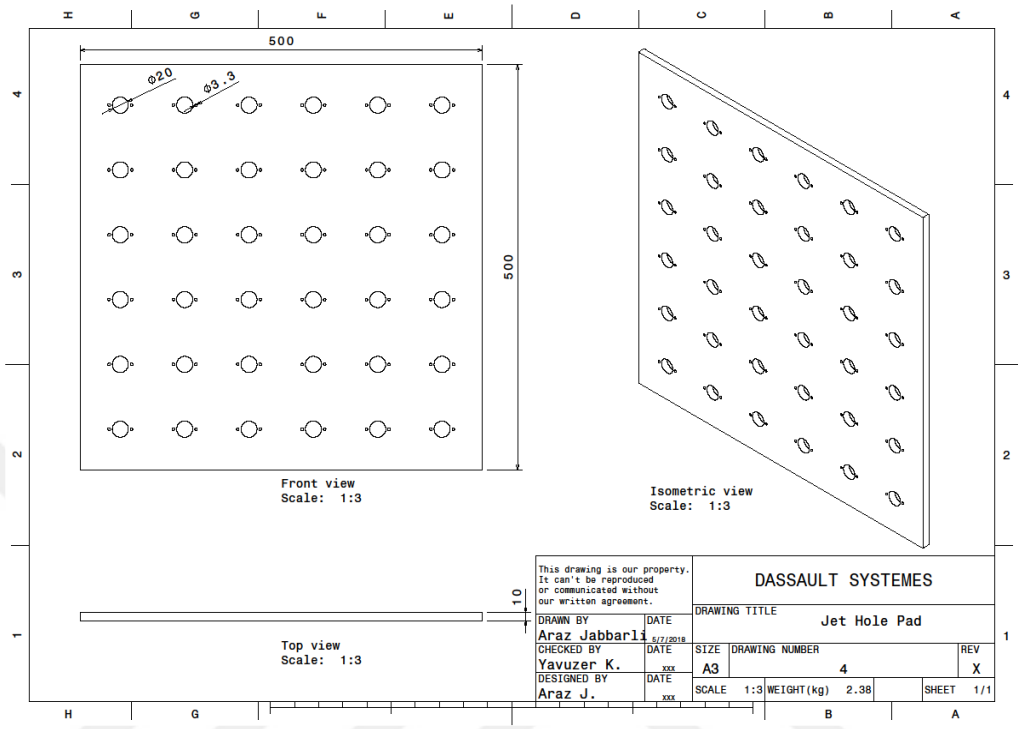

Figure A. 10 Jet hole pad

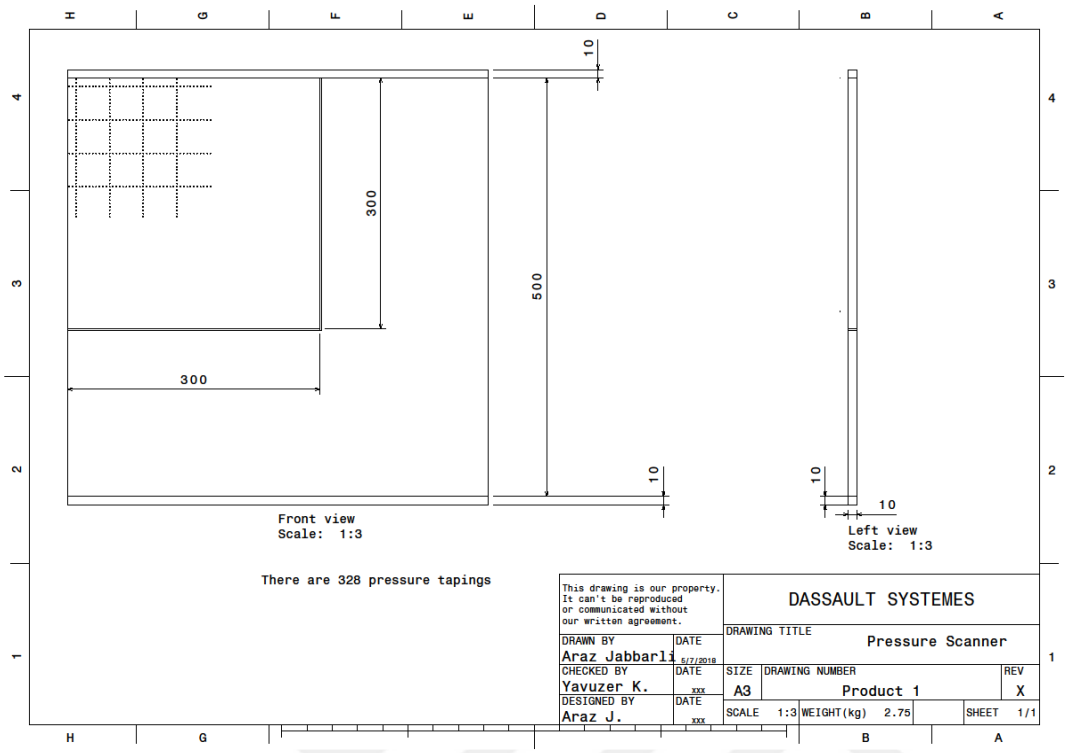

Figure A. 11 Pressure Scanner

APPENDIX B: Pressure distribution for H/d_n = 4 and 6 along the scanning line of C and D

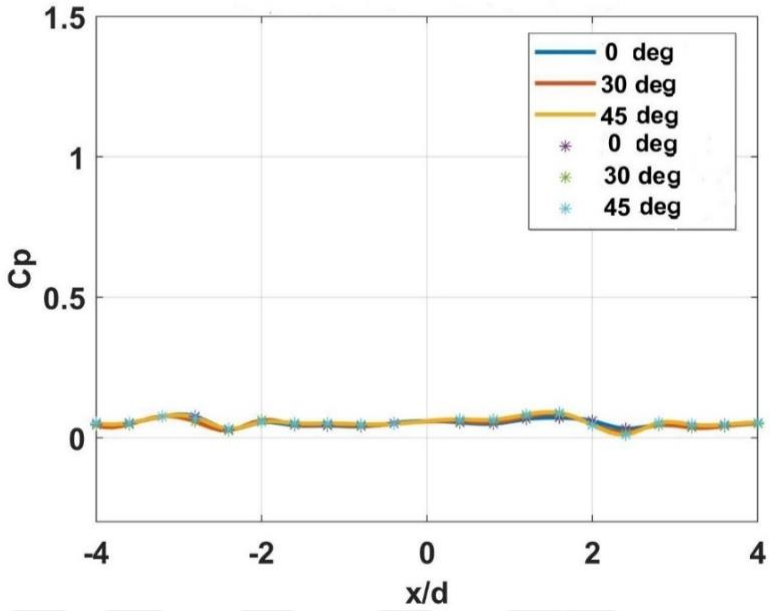

Figure B.1 H/d_n = 4 Re = 19200 – Pressure distribution along the line C

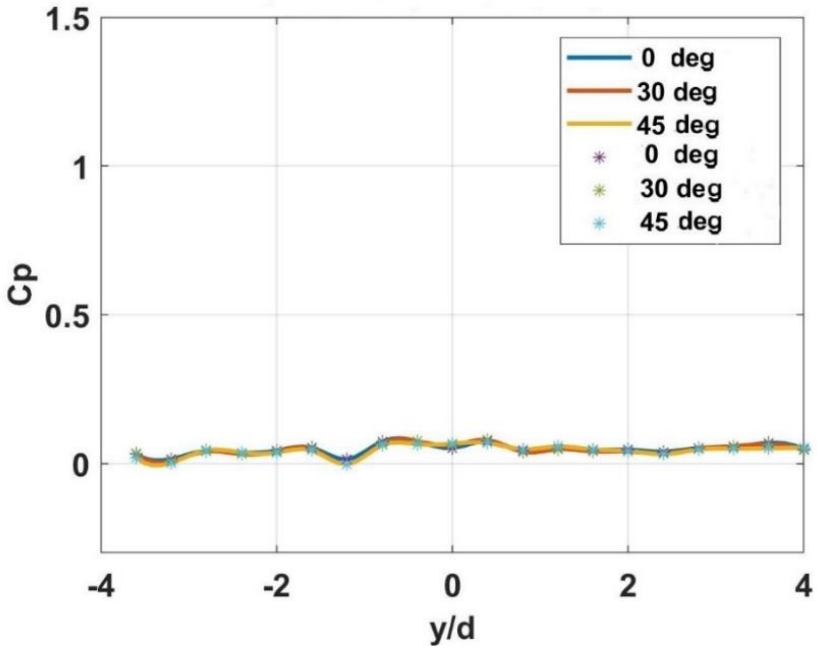

Figure B. 2 H/d_n = 4 Re = 19200 – Pressure distribution along the line D

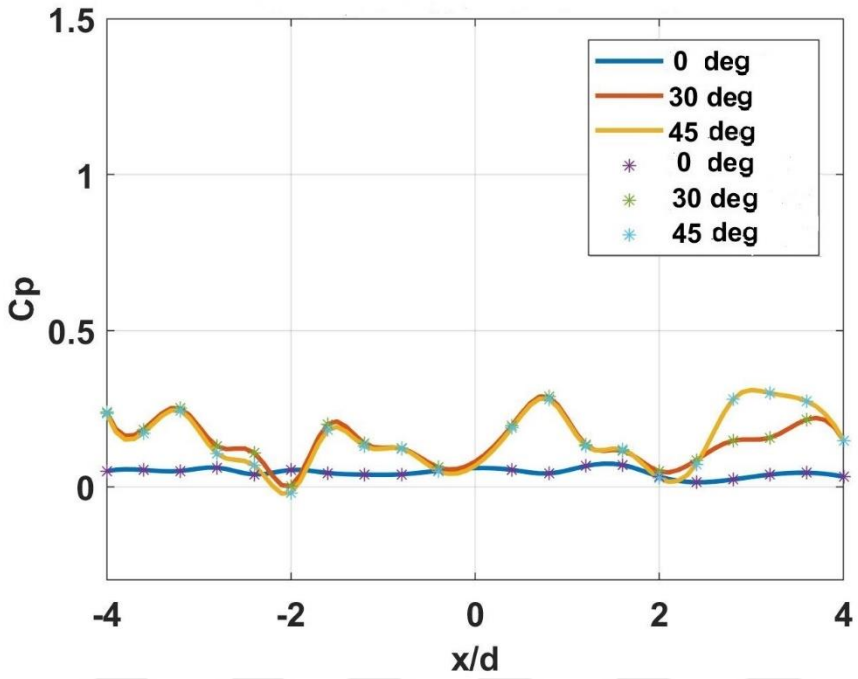

Figure B. 3 H/d_n= 6 Re = 19200 – Pressure distribution along the line C

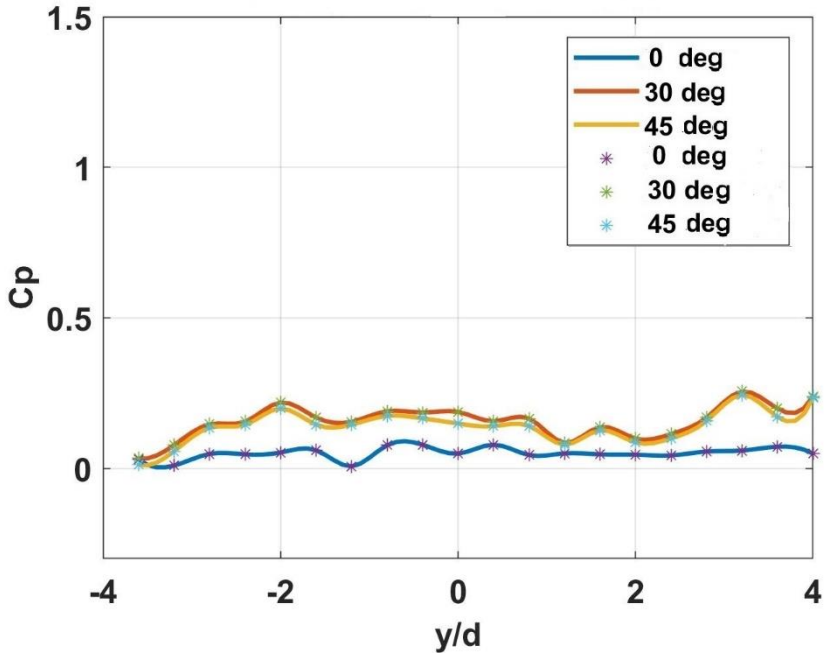

Figure B. 4 H/d_n= 6 Re = 19200 – Pressure distribution along the line D

7. CURRICULUM VITAE

Name Surname **:** Araz JABBARLI

Place and Date of Birth **:** Azerbaijan, Baku 08/01/1990

E-Mail **:** jabbarli15@itu.edu.tr

EDUCATION

- **B.Sc.** **:** Middle East Technical University, Aerospace Engineering

PROFESSIONAL EXPERIENCE AND REWARDS:

- Laureate of Erasmus Internship Mobility Grant Istanbul Technical University , 2017
- 2nd Place as a team (“Ghostbusters”) in Istanbul Technical University EBEC - European BEST Engineering Competetion